Terrain-Aided Navigation with Coarse Maps – Towards an Arctic Crossing with an AUV

Georgios Salavasidis, Andrea Munafò, Stephen D. McPhail, Catherine A. Harris, Davide Fenucci, Miles Pebody, Eric Rogers and Alexander B. Phillips

Abstract

The desire to conduct research in the Arctic on an ever-larger spatio-temporal scales has led to the development of long-range autonomous underwater vehicles (AUVs), such as the Autosub Long-Range 1500 (ALR1500). Whilst these platforms open up a world of new applications, their actual use is limited in GPS-denied environments since self-contained navigation remains yet unavailable. In response, this study evaluates whether terrain-aided navigation (TAN) can enable multi-month deployments using basic navigation sensors and sparse bathymetric maps. To evaluate the potential, ALR1500 undertakes a hypothetical science-driven mission from Svalbard (Norway) to Point Barrow (Alaska, USA) under the sea ice (a mission over 3200 km). Therefore, a simulated environment is developed which integrates a state-of-the-art model of water circulation, error models for heading estimation at high latitudes and an Arctic bathymetric map. Recognising that this map is constructed based on sparse depth measurements and interpolation techniques, a bathymetric uncertainty model is developed. The performance of the TAN algorithm is examined with respect to the type of the heading sensor utilised and a range of vertical map distortions, calculated using the developed bathymetric uncertainty model. Simulations show that unaided navigation experiences an error of hundreds of kilometres, whereas TAN provides acceptable accuracy given a moderate map distortion. By degrading the quality of the map further, it appears that the navigation filter may diverge when traversing large regions subject to interpolation. Therefore, a Rapidly-exploring Random Tree Star (RRT*) algorithm is used to design a new path such that the AUV traverses reliable and rich in topographic information areas.

Index Terms

G. Salavasidis (e-mail: geosal@noc.ac.uk), A. Munafò, S. McPhail, C. Harris, D. Fenucci, M. Pebody and A. Phillips are with the Marine Autonomous & Robotic Systems Group, National Oceanography Centre, Southampton, SO14 3ZH, UK.

E. Rogers is with the Department of Electronics and Computer Science, University of Southampton, Southampton SO17 1BJ, UK.

Terrain-aided navigation, underwater navigation, long-range autonomous underwater vehicles, under-ice navigation, polar vehicle operations

I. Introduction

The Arctic is the most rapidly changing environment on the planet [1], which has both local and global implications [2]. The rapidly receding ice cover together with an increase in maritime traffic and exploitation of marine resources are leading to a growing demand for accurate environmental prediction systems and weather forecast products in the Arctic [3].

Environmental models heavily rely on ocean observations [4], both in situ and from remote satellite sensing [5]. However, the Arctic presents a number of unique observing challenges [6] causing a significant gap in the Arctic observing systems and hindering the reliability in predicting the environmental dynamics [4]. Real-time (or near real-time) in situ observations, such as collected by Argo floats [7] or research ships, are limited due to the sea ice cover, whereas satellite services provide data of low resolution and accuracy due to, for example, difficulties in distinguishing snow and ice from clouds [8].

As a result, the dynamics of the physical environment in the Arctic and of the ecosystems within are currently poorly understood [9]. However, emerging maritime technologies can provide new cost-effective opportunities for obtaining subsea measurements and bridging the gap in knowledge [10]–[12]. For example, autonomous underwater vehicles (AUVs) are particularly useful mobile platforms for carrying science payload and collecting data from areas previously inaccessible unaffected by harsh weather conditions above the water [13]–[15].

In the open ocean, AUVs have been widely utilised for scientific, industrial and military purposes [16]–[19]. However, the Arctic poses new technological challenges for these vehicles [20]–[22]. The use of AUVs under the ice is currently extremely limited because the ice-cover restricts surface access preventing the vehicles from using satellite services for communication and navigation. As a result, the vast majority of the reported deployments in the Arctic have been short-term, i.e. lasting from few hours to few days (per deployment), typically because of the significant energy required by the navigation and science sensors (e.g. see [23], [24]), or short-range in the vicinity of an external acoustic-based support system [25], [26]. Consequently, basin scale experiments are currently only possible with manned submarines [27].

In response to the increasing demand for conducting subsea measurements on ever-larger temporal and spatial scales, long-range propeller-driven AUVs have been developed, such as the

Tethys [28] and the Solus [29]. Similarly, the National Oceanography Centre (NOC) in the UK has developed the Autosub Long-Range 6000 (ALR6000) [30] and the Autosub Long-Range 1500 (ALR1500) [31], which are specifically designed for basin scale under-ice operations. These platforms combine the extreme range already achievable by underwater gliders [32] with increased manoeuvrability, position control and payload capacity of large flight-style AUVs. By using high energy density lithium primary cells and minimising the energy consumption within all sub-systems, the vehicles can achieve a multi-month endurance [33], [34]. This capability coupled with the ample flooded space available and the increasing availability of low-power sensors have provided these vehicles with a variety of payload options and use cases.

However, deploying AUVs for a prolonged period of time in ice-covered environments comes with its own challenges. One key problem is the AUV navigation since GPS positioning is unreachable and long-range vehicles are normally limited to a small number of low-power navigation sensors causing an unaided navigation system to experience rapid error growth [35]. This problem further escalates during missions in extremely high latitudes, where heading sensors experience degraded performance [23], [33], and/or whilst operating mid-water column where the navigation that is influenced by water currents is presently the weakest [36].

To enable long-range missions under the sea ice with the ALR vehicles, a terrain-aided navigation (TAN) system has been developed providing a computationally feasible solution in real-time on processing boards with limited resources [34], [37], [38]. The system relies on basic low-power motion sensors and low-informative sonars to obtain bathymetric observations, such as the NOC's single-beam echo-sounder specifically developed and optimised for the ALR1500. Bathymetric observations are then correlated to a pre-existing bathymetric map in order to determine the vehicle's position within that map [39].

Whilst TAN has proven effectiveness [39]–[43], real-time applications are limited in number and typically rely on power-demanding sensors and high-resolution bathymetric maps (varying from a sub-meter resolution to up only few metres). Large scale, high-resolution bathymetric maps are rarely available though, particularly in remote deep oceans, and the reliance on energy-expensive sensors severely limits the AUV endurance. Therefore, currently the TAN applications are in majority short, ranging from hundreds of metres to few kilometres, and are concentrated in areas where detailed bathymetric maps pre-exist.

In contrast to the above, it was demonstrated in Salavasidis, *et al.* [33] that the TAN system of the ALR vehicles can deal with low-quality bathymetric grid maps and strong time-varying

water currents, despite using basic low-power sensors. The performance of the navigation system was evaluated using field data collected during three multi-day deployments of the ALR6000 in the Southern Ocean (with the longest mission, named M44 and shown in Fig. 1, exceeding 76 hours and covering $\approx$ 200 km range at depths of over 3500 m). This dataset forms a unique test case for assessing the TAN performance under extremely challenging conditions. Despite traversing areas with low topographic information during M44 and ignoring speed over the ground measurements, the TAN system limits the localisation error to within a few hundreds of metres by using a 50 m resolution bathymetric grid map (see A-C and G-I subplots in Fig. 1), as opposed to a dead-reckoning (DR) solution which experiences an error of over 40 km in three days ($\approx$ 76 hours) without bottom-lock information. To further evaluate the system performance under progressively degraded map quality, new bathymetric grid maps were generated with resolutions similar to the size of grid cells in typical digital bathymetric models of the world's oceans (100-400 m cell size [44]). Note that for generating these new grid maps significant bathymetric information was discarded by sub-sampling the original 50 m resolution map (see D-F subplots in Fig. 1 for M44). Despite this challenging setup, the navigation filter exhibited robust and relatively accurate behaviour during the total length of $\approx$ 370 km of all three missions in the Southern Ocean [33].

Given these promising results, this work assess in simulation whether TAN can be used in the Arctic for basin scale operations with ALR1500, where the bathymetric map is constructed using sparse measurements and interpolation. Therefore, a simulated environment of the Arctic is developed which integrates the Nucleus for European Modelling of the Ocean (NEMO) [46], a state-of-the-art model of ocean circulation; error models for heading estimation at high latitudes [33]; and a coarse bathymetric map of the Arctic Ocean, as constructed by the International Bathymetric Chart of the Arctic Ocean (IBCAO) project [47]. Recognizing that large regions of the map are subjected to pure interpolation, a bathymetric uncertainty model is developed which assigns a degree of reliance to each grid cells of the Arctic map. Using the resulting simulator, the TAN performance is evaluated with respect to several factors: a) the type of the employed heading sensor (which can be either a magnetic compass or a gyrocompass); b) a range of vertical distortions applied to the reference map (according to the developed bathymetric uncertainty model); and c) the characteristics of the pre-designed path of the vehicle.

The remainder of the paper is structured as follows: Section II presents the navigational challenge of crossing the Arctic with ALR1500. Section III briefly discusses the TAN system

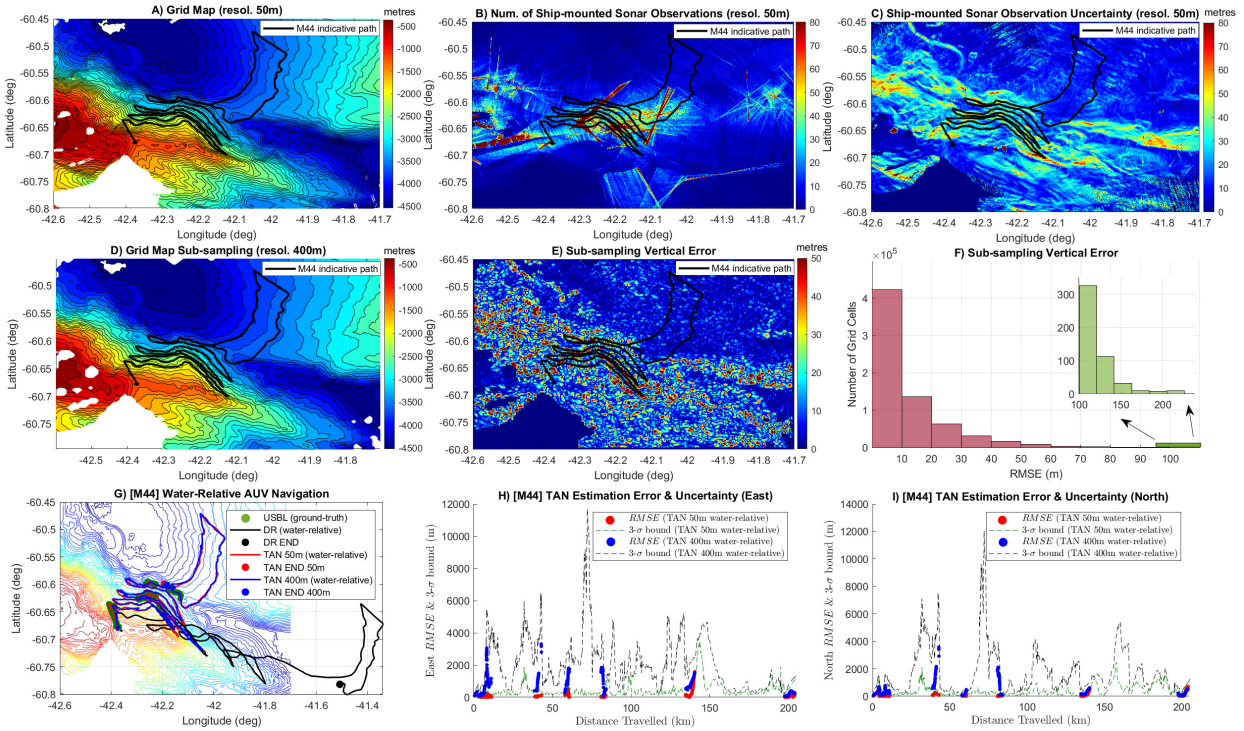

Fig. 1. ALR6000 deployment in the Southern Ocean in 2017 [33] and the bathymetric grid map of the area [45]. **A:** Bathymetric grid map of 50 m resolution constructed using ship-mounted multibeam sonar observations and spline interpolation (for gaps of up to 10 grid cells wide). **B:** Grid showing the number of ship-mounted sonar observations that fall within each bathymetric grid cell in **A**. **C:** Grid showing the vertical standard deviation of the ship-mounted sonar observations that fall within each bathymetric grid cell in **A**. This subplot illustrates one of the error sources in bathymetric models when using a grid representation of the seafloor. **D:** Bathymetric grid map of 400 m resolution constructed after sub-sampling the original grid map in **A**. **E:** Grid showing the vertical error introduced by sub-sampling the grid map in **A** to construct the grid map in **D**. To facilitate direct comparisons, the low-resolution grid map is re-scaled back to original resolution via bi-linear interpolation. **F:** Histogram enumerating grid cells that fall into range of vertical error (expressed as root mean square error) introduced by sub-sampling the grid map in **A** to construct the grid map in **D**. **G:** AUV path as estimated using DR navigation (black) or TAN (red/blue for 50/400 m resolution grid map, respectively) during M44 when ignoring speed over the groud measuremens (water-relative navigation). The vehicle's baseline position, shown in green, is intermittently recorded by the ship's ultra-short baseline (USBL) positioning system. The path estimates are visualised over the original bathymetric grid map. **H & I:** TAN estimation error, with respect to the USBL measurements (when available), over distance travelled with the corresponding 3-σ bound in the north and east directions during M44 (when employing the original bathymetric grid map or the degraded one).

and develops an uncertainty model for the bathymetric map of the Arctic Ocean. Following, Section IV details the simulated environment of the Arctic which is used in Section V to numerically evaluates the TAN performance with respect to the several factors. To improve the navigation performance, Section VI uses a Rapidly-exploring Random Tree Star (RRT*)

algorithm [48] to optimise the path of the vehicle. Finally, Section VII summarises the work presented and provides future research directions.

II. Proposed Arctic Crossing

To assess the potential for TAN to address the localisation challenge for Arctic Basin scale AUV operations, a hypothetical mid-water column crossing (i.e. navigation relative to the water mass) from Svalbard (Norway) to Point Barrow (Alaska, USA) is considered as shown in Fig. 3. This equates to a nominal range of 3200 km operation in a GPS-denied environment.

This route for the vehicle is designed to fulfil two basic requirements: maximising the distance from heading sensor-dependent critical regions (the Magnetic North Pole when using a magnetic compass and the Geographic North Pole when using a gyrocompass) and avoiding traversing the featureless terrain of the Canada Basin (yet keeping the path relatively short), which is particularly important for successfully applying TAN [49]. This route is also similar to that undertaken by British submarine Tireless in March 2007, which enabled the thickness characteristics of the ice cover to be measured during the winter immediately preceding the exceptional ice retreat of summer 2007 [27].

The ALR1500 operates at a constant forward speed (0.6 m/s) and depth (1000 m) in the simulated environment of the Arctic, as detailed in Section IV. The minimum navigational requirement for this mission is to maintain the positioning error bellow 100 km throughout the entire route. This allows the AUV to maintain sufficient accuracy during the transit to avoid danger, and to surface in an ice-free area of the Barrow coast (which depends on the seasonal ice extent) for recovery.

A. ALR1500: a long-range AUV for polar operations

ALR1500 [31] is a novel flying-style propeller-driven AUV designed based on the proven architecture of ALR6000 [30], [50], [51] (see Fig. 2), but with significantly extended endurance [33]. The vehicle can be powered by Bobbin-type lithium-thionyl chloride primary cells, which have very low self-discharge rates making them suitable for long-range deployments. ALR1500 is able to carry 28 battery packs with each in 7s8p cell configuration, resulting in a total potential energy over 107 kWh [33], [34]. This translates into a range of over 6000 km (see [33], [34]) when operating at the optimum forward speed ($\approx$ 0.5 m/s) and using the basic navigation sensor suite (described in Section II-B).

Fig. 2. Autosub Long-Range 1500 front and Autosub Long-Range 6000 behind.

B. ALR1500: navigation system and sensor suite

The navigation sensor suite of ALR1500 is limited to a small number of low-power sensors normally including: a GPS module to obtain position fixes when at the surface; a 6-axis magnetic compass/attitude module for heading estimation; a conductivity, temperature and depth (CTD) probe to calculate the operating depth using the UNESCO pressure-to-depth conversion algorithm [52]; and two acoustic doppler current profilers (ADCPs) facing upwards and downwards. The downward-facing ADCP is used to estimate velocity (bottom- or water-relative) and to provide range-to-bottom measurements when operating near bottom, whilst the upward-facing ADCP is primarily used for avoiding collision with the sea ice from above. To level the velocity vector in a local horizontal reference frame, the downward-facing ADCP is integrated with tilt sensors, micro-electro-mechanical system accelerometers. Moreover, ALR1500 can further be equipped with the a north-seeking fiber-optic gyrocompass (FOG) for more reliable heading estimation. Assuming the use of the Octans gyrocompass, which requires approximately 18 W [53], the

projected range of the vehicle drops to approximately 3600 km [33], which is still sufficient for traversing the Arctic Basin.

For navigation, ALR1500 dead-reckons using a 2D motion model (piecewise constant velocity), a process which is initialised by GPS whilst the vehicle at the surface, and several algorithms for real-time sensor calibration [13], [38]. However, the unavoidable errors in the motion sensors result in an unbounded error growth. The main error sources are the water currents (if unobservable) and the inaccuracies in heading estimation. The former introduces a substantial positioning drift when the speed of the vehicle is of the same order as the current velocity, whereas the latter becomes important during operations at high latitudes where heading sensors have degraded performance [23], [33]. Fig. 3 shows the regions where the heading sensors are expected to be unreliable (note that the highlighted no-go zones are by no means an exact quantification of the regions to be avoided, but rather a visualisation of the areas with high risk). Multi-day experiments in the deep Southern Ocean have shown that the DR error for the Autosub Long-Range family of vehicles is approximately 1% of distance travelled (DT) when using speed estimates over the ground [38], whereas the error is proportional to the speed of the water currents when navigating relative to the water column [37].

For applications requiring enhanced navigation accuracy, or where the long-term error may be significant, ALR1500 can use TAN techniques to limit the navigation error [34]. Deployments near the seabed can benefit from using range measurements available by the downward-facing ADCP [38]. For deployments out of the ADCP's bottom tracking range, ALR1500 can further be integrated with a bespoke 4000 m range 12 kHz single-beam echo-sounder developed in the NOC. To minimise the energy requirements, the echo-sounder has been designed to function at a low repetition rate (of the order of minutes), and has been optimised to have low quiescent power demand and minimum possible volume to fit in the ALR1500.

C. Crossing the Arctic Ocean with ALR1500 and Dead-Reckoning Navigation

Fig. 3 with simulated crossings of the Arctic (detailed in Section IV) shows that DR navigation[1] may experience an error up to 420 km at the surfacing location (Point Barrow) when using a gyrocompass, whereas the error may grow up to 2400 km by using the magnetic compass for heading estimation. By isolating the navigation error sources, it appears that the drift caused by

[1]The interested reader is referred to [34] and [38] for an in-depth description of the ALR1500's DR algorithm.

the water currents, as obtained by the NEMO model for a certain (but random) spatio-temporal instance at 1000 m depth during winter months, is approximately 40 km. Hence, the DR error appears to be in the majority driven by the heading errors in these simulated experiments at this specific operating depth. However, note that the these simulated experiments are configured in a way aiming to realize the worst possible navigation scenario, hence heading errors may have significantly been overestimated due to the intrinsic difficultly to predict the performance of heading sensors in Arctic (further details are given in Section IV-B). This worst-case setup essentially provides an estimate of the upper error bound for DR navigation, provided that the spatio-temporal instance of the NEMO model is a good representation of the typical water currents present in the Arctic Ocean. Given this, it is to be expected that the actual DR error for this specific path will always fall within a circle centred at the true position of the vehicle (Point Barrow) with radius specified by the calculated navigation error, which is 420 km when using a gyrocompass and is 2400 km when using a magnetic compass.

Based on these results, it is clear that there is a high risk for permanent vehicle loss under ice when using DR. Therefore, alternative navigation solutions must be investigated.

III. Terrain-Aided Navigation in the Arctic Ocean

The TAN system developed in the NOC for sensor-limited AUVs uses the Rao-Blackwellised particle filter (RBPF) for state estimation [34], [54], [55]. This is because of its ability to represent an arbitrary state posterior probability density function (i.e. dealing efficiently with non-linearities) whilst maintain the computational demand reasonably low. The latest is achieved by modelling and estimating a relatively low-dimensional state vector [37].

A. Process Model

For real-time applications, the filter state tracks the northing and easting position of the vehicle, which are recorded in radians of latitude and longitude (LL), respectively. The state vector also includes velocity biases in north and east direction. For well-calibrated navigation sensors, the bias sub-state effectively tracks the speed of the water currents in order to compensate for the water flow when accessing only water-relative velocity measurements. However, these velocity biases can also capture the impact of a slow-varying heading bias, provided that the vehicle maintains a relatively steady direction of motion (which further allows us to reduce the error complexities and keep the dimension of the estimation problem low).

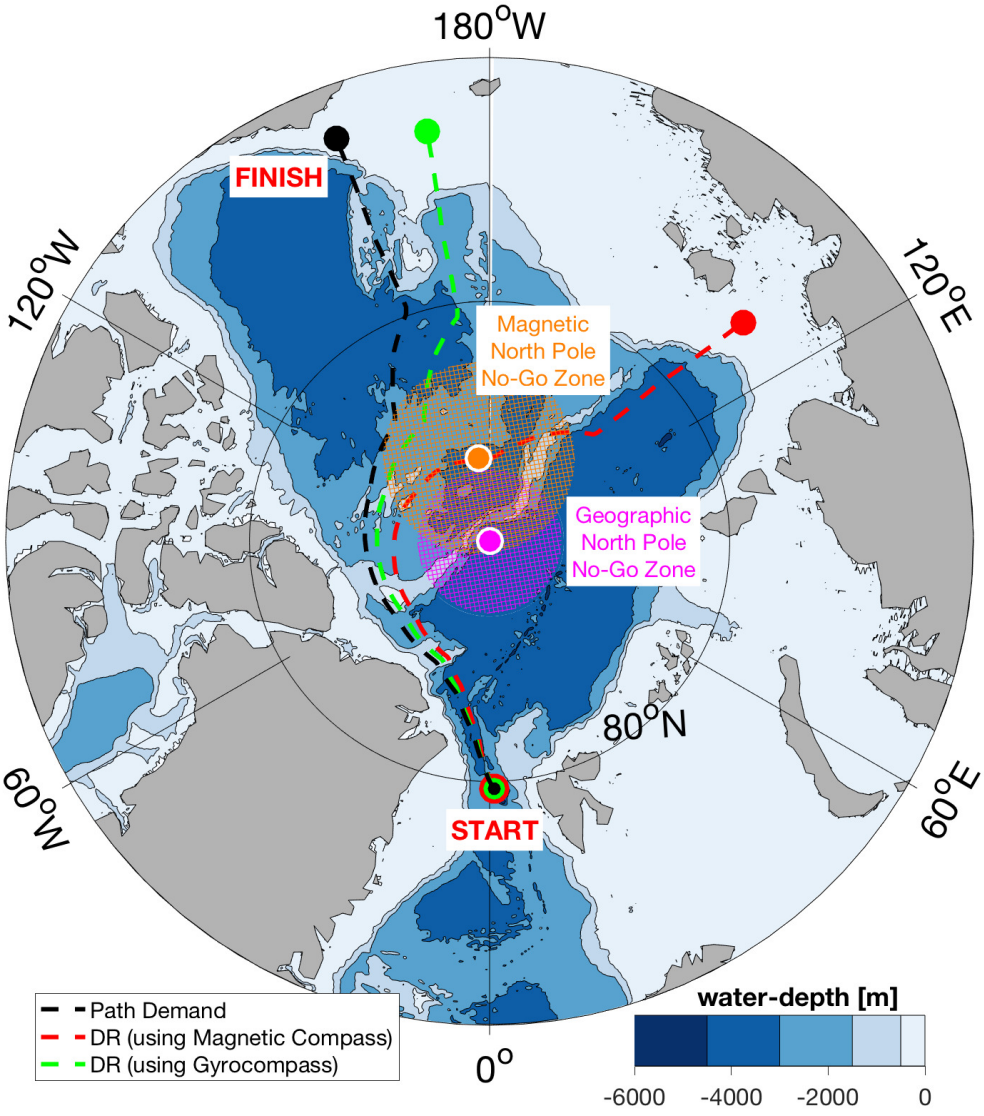

Fig. 3. One possible route (≈ 3250 km) to traverse the Arctic Ocean with ALR1500. The designed path maximises the distance from sensor-critical latitudes whilst avoiding the morphologically flat Canada Basin. The black line shows the demanded (true) path, whereas the red and green lines represent the paths estimated by DR navigation when using a magnetic compass or a gyrocompass for heading determination, respectively. The simulation setup aims at approximating the worst possible navigation scenario (see details in section IV-B).

Velocity biases are modelled as a random walk with low-intensity Gaussian step per direction, whilst the vehicle's motion is modelled by a discrete Markov process that relies on 2D kinematics. This propagates position estimates forward in time by integrating water-relative

velocity, $\boldsymbol{u}_k = [u_k^N, u_k^E]^T$, expressed in a local north-east-down navigation frame. The latter is obtained by rotating body frame velocity measurements provided by the downward-facing ADCP. The mathematical expression for the discrete-time process model is given by [37]:

$$\left[\begin{array}{c} \boldsymbol{x}_{k+1} \\ \hdashline \boldsymbol{b}_{k+1} \end{array}\right] = \left[\begin{array}{c:c} I_{2\times2} & F(\boldsymbol{x}_k) \\ \hdashline 0_{2\times2} & I_{2\times2} \end{array}\right] \left[\begin{array}{c} \boldsymbol{x}_k \\ \hdashline \boldsymbol{b}_k \end{array}\right] + \left[\begin{array}{c:c} F(\boldsymbol{x}_k) & 0_{2\times2} \\ \hdashline 0_{2\times2} & 0_{2\times2} \end{array}\right] \left[\begin{array}{c} \boldsymbol{u}_k \\ \hdashline 0_{2\times1} \end{array}\right] + \left[\begin{array}{c} \boldsymbol{\eta}_k^{\boldsymbol{x}} \\ \hdashline \boldsymbol{\eta}_k^{\boldsymbol{b}} \end{array}\right], \quad \text{with: } F(\boldsymbol{x}_k) = \Delta t \begin{bmatrix} R_e^{-1} & 0 \\ 0 & \left(R_e \cdot \cos(x_k^{Lat})\right)^{-1} \end{bmatrix} \tag{1}$$

where $\boldsymbol{x}_k = [x_k^{Lat}, x_k^{Lon}]^T$ is the LL position in radians at time k; $\boldsymbol{b}_k = [b_k^N, b_k^E]^T$ is the velocity bias vector with components in north and east direction (expressed in m/s); Δt is the position propagation period, during which $\boldsymbol{u}_k$ and $\boldsymbol{b}_k$ are assumed to be constant; $F(\boldsymbol{x}_k)$ is a transformation matrix used to convert the north and east displacement during Δt to the corresponding displacement in LL; R_e is the radius of Earth in metres; and the vectors $\boldsymbol{\eta}_k^{\boldsymbol{x}} = [\eta_k^{Lat}, \eta_k^{Lon}]^T$ and $\boldsymbol{\eta}_k^{\boldsymbol{c}} = [\eta_k^N, \eta_k^E]^T$ correspond to the process noise. $\boldsymbol{\eta}_k^{\boldsymbol{x}}$ represents model mismatches expressed in radians and follows normal distribution $\mathcal{N}(0, Q_k^{\boldsymbol{x}})$. Similarly, $\boldsymbol{\eta}_k^{\boldsymbol{b}}$ is used to account for spatio-temporal variations in the velocity biases and follows $\mathcal{N}(0, Q_k^{\boldsymbol{b}})$. The intensity of this noise is typically low and it is expressed in m^2/s^2. Note that by vanishing the noise terms and the velocity bias, the process model in (1) becomes the exact position propagation model used by the ALR1500 for dead-reckoning.

B. Observation Model

The NOC's single-beam echo-sounder can realize range measurements at approximately one-minute repetition rate even when operating mid-water in deep oceans. The sonar beam orientation is normally perpendicular down towards the seabed and here we also assume, for simplicity, that the vehicle is perfectly stabilised in pitch and roll (otherwise each range measurement must be compensated for the attitude of the vehicle and the beam orientation to find where the beam precisely hits the bottom [37]). Then, the water depth (z_k) at time k can be computed on-board the vehicle, which is located at $\boldsymbol{x}_k$, as the sum of the derived operating depth (d_k) and the measured range (r_k): $z_k = r_k + d_k$; with all quantities expressed in metres.

Bathymetric observations can be modelled using a function that relates $\boldsymbol{z}_k$ to the water depth at $\boldsymbol{x}_k$:

$$z_k = \bar{h}(\boldsymbol{x}_k) + \omega_k, \tag{2}$$

where $\bar{h}(\boldsymbol{x}_k)$ provides the true water depth at $\boldsymbol{x}_k$ and ω_k is the observation noise, assumed to follow $\mathcal{N}(0, \sigma^2_{\omega_k})$, aiming to represent the combined effect of the errors in r_k and d_k [34]. However, in reality the true bathymetry $\bar{h}(\cdot)$ is unknown and only a non-linear terrain model, $h(\cdot)$, is available for use (typically in the form of a uniform grid map). Hence, $h(\cdot)$ represents the true seabed to some varying degree of accuracy and the vertical deviation of each grid cell from the reality constitutes an error. This spatially varying error can be expressed as: $m(\boldsymbol{x}) = h(\boldsymbol{x}) - \bar{h}(\boldsymbol{x})$; and for this study $m(\boldsymbol{x})$ is assumed to follow $\mathcal{N}\big(0, \sigma^2_m(\boldsymbol{x})\big)$ as per [37] and the results in Fig. 1. While this assumption is perhaps simplistic, results have shown the navigation filter is robust to complex map errors, including large biases that are hard to be explicitly modelled.

Given the above assumption, the following discrete time function can be used to model bathymetric observation:

$$z_k = h(\boldsymbol{x}_k) + \overbrace{\zeta_k}^{\omega_k + m(\boldsymbol{x}_k)}, \tag{3}$$

where $h(\cdot)$ relates the bathymetric map at $\boldsymbol{x}_k$ to the on-board observation z_k and ζ_k aims to capture the overall impact of the errors in the bathymetric map together with those in the sensors involved. Given the assumptions of normality and statistical independence between the error sources, ζ_k follows $\mathcal{N}(0, \sigma^2_{z_k})$ with σ_{z_k} to be given by:

$$\sigma_{z_k} = \sqrt{\sigma^2_{\omega_k} + \sigma^2_m(\boldsymbol{x}_k)}, \tag{4}$$

hence σ_{z_k} is dependent on the quality of the employed bathymetric map and the accuracy of the sensors involved. Further details about modelling errors and quantifying uncertainties are given in the following subsection (III-C and III-E). Note also that although more complex sensor error models can be considered, it is to be expected that unmodelled error will have negligible effect when compared to errors in sparse bathymetric maps.

C. Arctic Ocean Bathymetry

The bathymetric map of the Arctic Ocean is obtained from the IBCAO project. Using an accumulated database containing all available bathymetric data north of 64° and state-of-the-art oceanographic techniques, IBCAO has constructed a grid model of the Arctic Ocean. This grid is compiled from a mixture of data sources ranging from single- and multi-beam soundings with available metadata from past and modern expeditions to spot soundings with no available metadata, digitised contour maps (isobaths), published hydrographic charts, and depth models.

The constant increase of bathymetric data, e.g. from icebreaker cruises and declassified echo soundings acquired by submarines, has led to the latest release that consists of a terrain model on a polar stereographic projection with a grid cell spacing of 500 m $\times$ 500 m (or a re-projected version with 30 arcsec $\times$ 30 arcsec). However, the pace at which the Arctic Ocean is getting mapped is very slow and only 11% of the Arctic Ocean is actually covered by multi-beam surveys [47]. Regions where no bathymetric measurements exist are filled using interpolation.

Sources of error (and thus of uncertainty) in bathymetric maps are typically grouped into three wide categories [56], [57]: *Type 1* - depth measurement errors (e.g. uncompensated biases and positional inaccuracies) and temporal changes (ageing of sounding data); *Type 2* - errors introduced when processing available depth measurements with gridding algorithms to create grid models (e.g. numerical errors, errors introduced by averaging/smoothing and interpolating, see e.g. A-C subplots in Fig. 1); and *Type 3* - errors due to the terrain variability within each grid cell and between the available depth measurements. Therefore, the uncertainty associated with each grid cell depends on that in the depth measurements and the gridding techniques utilised, together with the topographic variability. High-resolution grid models are primarily affected by *Type 1* errors, whereas low-resolution maps containing large regions with depth values subjected to interpolation can be massively affected by errors of *Type 2* and *Type 3*. Fig. 4 shows schematically the vertical uncertainty of a bathymetric map.

A common and widely used approach to quantifying the vertical bathymetric uncertainty is to use a single global (i.e. space-invariant) measure of deviation, such as the root mean square error (RMSE) or standard deviation statistics [58]. While this oversimplified error representation can be adequate for easily accessible shallow waters where high resolution maps can be developed (predominantly affected by errors of *Type 1*), it is insufficient to account for the spatial variation of the map error in remote deep oceans where the map resolution dramatically decreases. The IBCAO grid map contains large areas where depth values are filled via interpolation, or using digitised isobaths derived from classified mapping missions (for which the data quality is unknown). This inevitably introduces large errors of *Type 2* and *Type 3* that, in addition, can significantly vary with space and thus requiring complex space-varying error representations. Although developing such models can be a very challenging task [58], particularly for the Arctic Ocean [59], they are necessary to avoid underestimating or overestimating the map errors, in which cases TAN would either fail (case underestimation) or experience degraded performance in well-mapped regions (case overestimation).

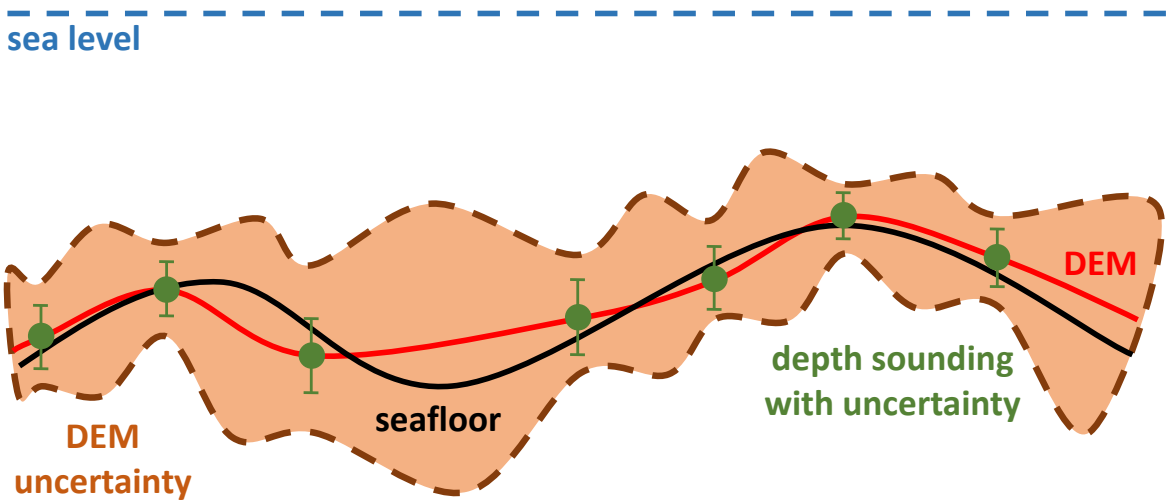

Fig. 4. Vertical bathymetric uncertainty (dashed-line) in 1D representation. The bathymetric map error is represented by the deviation of the model surface (red line) from the true seafloor (black line). The overall map uncertainty is a combination of uncertainties in depth measurements (e.g. sonar measurements) and the uncertainty associated with the gridding algorithm (e.g. spatial interpolation). Notice that measurements acquired from deeper waters are experiencing higher errors and uncertainties. The map also experiences increased uncertainty in wide regions unconstrained by depth measurements, where interpolation techniques are used to create the model surface.

1) Quantifying the Uncertainty in the Arctic Bathymetry Map: For the purpose of the crossing the Arctic Ocean using TAN, a standard deviation grid map is constructed quantifying the vertical bathymetry uncertainty in the IBCAO grid map. This effectively assigns an error standard deviation to each grid cell of the bathymetric map based on the source identification (SID) grid compiled by the IBCAO project. The SID grid allows the users of the IBCAO map to identify the dominating source used to derive the depth value of each grid cell. Given seven data sources, the SID grid contains seven codes distinguishing between data sources, which are categorized as: land (code 0); multi-beam sonar data (code 1); single-beam sonar data (code 2); Olex[2] data (code 3); contour lines from digitised maps (code 4); and other gridded bathymetric compilations (code 5) [47]. Grid cells subject to interpolation are originally labelled with a NaN; however,

[2]A seafloor mapping, navigation, and fishery system manufactured, by a Norwegian company, to interface with both single and multi-beam echo sounders.

for notation simplicity, they will be labelled with code 6. For the subsequent analysis, it is convenient to define a function which relates grid cells with the associated source code as:

$$\text{code}(\boldsymbol{x}) = \{0, 1, 2, 3, 4, 5, 6\},$$

where, $\text{code}(\boldsymbol{x})$ gets the code value that corresponds to the grid cell at $\boldsymbol{x}$.

Fig. 5 shows the SID grid after having compactly grouped the source data in order to show that the Arctic Ocean is primarily subjected to interpolation.

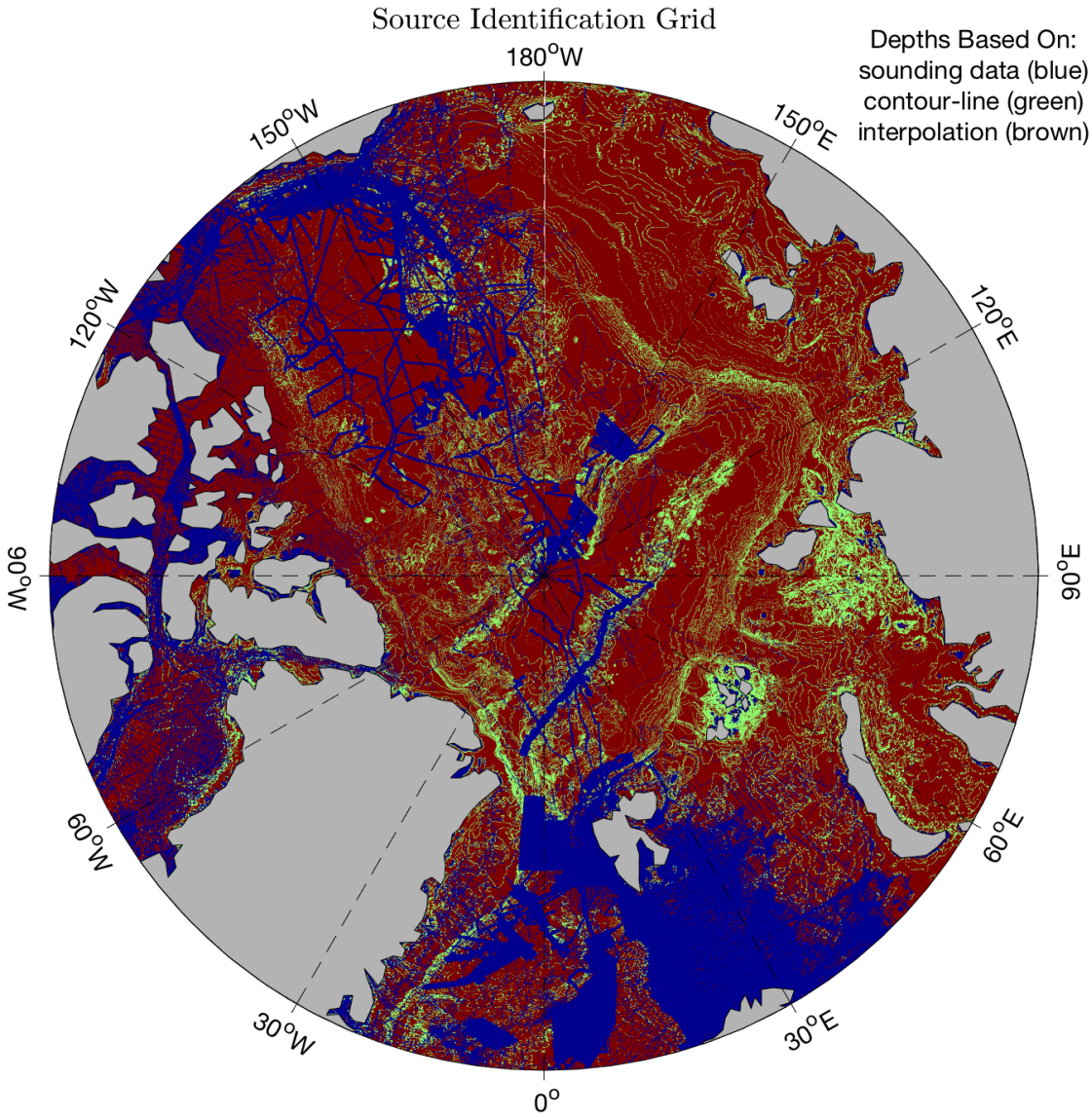

Fig. 5. SID grid map provided by the IBCAO project [47]. Sources of data are further grouped for easier visualisation. Note that sounding data of only a few grid cells wide are not distinguishable due to the map scale.

Grid cells corresponding to land are set to zero standard deviation. This can mathematically be expressed as:

$$\sigma_m(\boldsymbol{x}) = 0 \cdot h(\boldsymbol{x}), \quad \forall\ \boldsymbol{x} \ \text{ s.t. } \ \text{code}(\boldsymbol{x}) = \{0\}, \tag{5}$$

where $h(\boldsymbol{x})$ is the depth value of the terrain model at $\boldsymbol{x}$ and $\boldsymbol{x}$ corresponds, in this particular case, to a land surface $\big(\text{code}(\boldsymbol{x}) = \{0\}\big)$.

For the grid cells with depth values constrained by sonar measurements, $\big(\text{code}(\boldsymbol{x}) = \{1, 2, 3\}\big)$, the uncertainty is calculated following the sonar error model developed in [60]. This work evaluated the quality of old (pre-1969) and new (post-1968) deep ocean single- and multi-beam measurements using a collection of high-quality depth measurements from multi-beam surveys overlapping with the archival under evaluation dataset. Although the errors in sounding data appeared to be not truly Gaussian (e.g. due to the presence of outliers), the vast majority of the detected errors followed distributions close to normal. Based on this, the error in the archival sounding data has been expressed via a zero-mean Gaussian distribution and standard deviation that takes into account the uncorrelated errors in travel time, the sound velocity, and the terrain morphology (to additionally consider that archival sonar data may have been georeferenced inaccurately). Using the results from this study, the uncertainty of the depth values derived from sounding data is computed by:

$$\sigma_m(\boldsymbol{x}) = \sqrt{\varrho^2 + \Big(\xi \cdot h(\boldsymbol{x})\Big)^2 + \Big(\gamma \cdot s(\boldsymbol{x})\Big)^2}, \quad \forall\ \boldsymbol{x} \ \text{ s.t. } \ \text{code}(\boldsymbol{x}) = \{1, 2, 3\}, \tag{6}$$

where $s(\boldsymbol{x})$ is the slope of the grid cell at $\boldsymbol{x}$ for which the depth value is derived using sonar measurements ($\text{code}(\boldsymbol{x}) = \{1, 2, 3\}$). $\{\varrho, \xi, \gamma\}$ are parameters calculated in [60] by fitting the standard deviation of the sounding data to best-fit a Gaussian quantile-quantile analysis over the middle 95% of the data. For the post-1968 sounding data, the results obtained from the fitting process are: $\{\varrho$ = 1 m, ξ = 0.005 (0.5%), γ = 200 m$\}$, which are hereafter used. For the slope calculation, the neighbourhood method is used [61].

Judging the quality of the depth values derived from digitised contour maps and other depth models, $\big(\text{code}(\boldsymbol{x}) = \{4, 5\}\big)$, is not straightforward. In reality contour lines are typically interpolations based on, for instance, underlying sparse ship track data. Hence, contour maps are accurate only where the contour lines intersect with track lines. Therefore, without accessing source data and associated metadata, it is challenging to produce error estimates. Moreover, old manually created contour maps have also inherited the styles of the cartographer who drew

them, which further complicates the determination of uncertainty. Although the IBCAO project aims to minimize the use of digitised contour maps and depth models, there still exist depth values computed using these depth sources. A simple approach for quantifying the uncertainty in the contour-derived grid cells could be to assume a vertical error of up to 5% of the derived depth [59]. However, given that depth values based on these sources can be highly unreliable, it is preferred to treat them as if they were computed via interpolation (worst case scenario—discussed next).

Topographic interpolation techniques and the associated uncertainties have been a subject of particular interest in the geostatistical community over the years, a detailed review of various approaches can be found in [61]. However, the calculation of the impact of interpolation in large scale bathymetric maps yet remains a challenge. Studies indicate that the interpolation uncertainty predominantly and inversely depends on the terrain complexity [62], followed by the density and the spatial coverage of the available sonar measurements nearby. Interpolation techniques introduce lower errors in areas of low relief due to the higher degree of spatial dependence (autocorrelation) between depth measurements and the depth of nearby cells requiring interpolation. The opposite holds in areas of complex terrain morphology, where interpolations introduce greater errors as the interpolation-derived cells can deviate more from nearby depth measurements. Therefore, morphometric parameters, such as slope and curvature, can be used as predictors of the magnitude of the uncertainty introduced by interpolations.

For the IBCAO map and the grid cells subject to interpolation, a conservative uncertainty model is developed. As the spatial dependence reduces with distance (or, alternatively, the variogram increases), grid cells requiring interpolation experience growth in uncertainty proportional to the distance from grid cells constrained by sonar measurements (referred to as reference cells). The rate of the uncertainty growth is defined by the maximum expected terrain slope in the Arctic (worst-case scenario). Excluding land and very shallow water environments, it appears that the maximum slope, s_{max}, is 59° and is located along the Lomonosov Ridge. The uncertainty of a grid cell subject to interpolation inherits the uncertainty of the closest reference cell and is further increased (assuming statistical independence) proportionally to the distance between the two grid cells and the maximum expected terrain slope, which can mathematically be expressed

as:

$$\sigma_m(\boldsymbol{x}) = \sqrt{\left(\sigma_m(\boldsymbol{x}_j)\right)^2 + \left(\frac{\mathrm{dist}(\boldsymbol{x}, \boldsymbol{x}_j)}{3} \cdot \tan(s_{max})\right)^2}, \quad \forall\ \{\boldsymbol{x_j}, \boldsymbol{x}\} \text{ subject to: } \mathrm{code}(\boldsymbol{x}) = \{4,5,6\} \text{ and } \mathrm{code}(\boldsymbol{x}_j) = \{0,1,2,3\}, \tag{7}$$

where $\boldsymbol{x}_j$ refers to location of the closest reference cell to the grid cell subject to interpolation at $\boldsymbol{x}$ and $\mathrm{dist}(\boldsymbol{x}, \boldsymbol{x}_j)$ corresponds to the distance between the interpolated cell at $\boldsymbol{x}$ and the reference cell at $\boldsymbol{x}_j$, expressed in metres. It is further assumed that the uncertainty of the interpolated grid cells can be expressed by a zero-mean normal distribution with intensity computed using the 3-σ rule of the maximum expected error $\{\mathrm{dist}(\boldsymbol{x}, \boldsymbol{x}_j) \cdot \tan(s_{max})\}$. Note that grid cells with depth values derived from contour maps and depth models are treated as if they were subjected to interpolation.

Having defined the standard deviation for each possible source of depth data, the full standard deviation model can be summarised as:

$$\sigma_m(\boldsymbol{x}) = \begin{cases} 0 \cdot h(\boldsymbol{x}), & \text{if } \mathrm{code}(\boldsymbol{x}) = \{0\} \\ \sqrt{\varrho^2 + \left(\xi \cdot h(\boldsymbol{x})\right)^2 + \left(\gamma \cdot s(\boldsymbol{x})\right)^2}, & \text{if } \mathrm{code}(\boldsymbol{x}) = \{1,2,3\} \\ \sqrt{\left(\sigma_m(\boldsymbol{x}_j)\right)^2 + \left(\mathrm{dist}(\boldsymbol{x}, \boldsymbol{x}_j) \cdot \tan(s_{max})/3\right)^2}, & \text{if } \mathrm{code}(\boldsymbol{x}) = \{4,5,6\}, \\ & \text{with } \mathrm{code}(\boldsymbol{x}_j) = \{0,1,2,3\} \end{cases} \tag{8}$$

However, by constructing the entire bathymetric uncertainty grid map, it appears that the bathymetric uncertainty model penalises heavily even those grid cells subject to interpolation that are relatively close to the reference grid cells. This results in extreme values of uncertainty in large regions where depth values are unconstrained by sonar measurements. To make the bathymetric uncertainty grid map realistic, a set of lower values for the maximum terrain slope is considered (in addition to the maximum of $59°$). For example, Fig. 6 shows the bathymetric uncertainty grid map calculated for $s_{max} = \{5°, 15°, 30°, 59°\}$.

2) Placing an Upper Uncertainty Bound: Despite the reduction in the value of the terrain slope, unrealistically large uncertainties are still present. To eliminate these values, an upper bound for the bathymetry uncertainty needs to be placed. This error bound is possible and justifiable thanks to advances in satellite technology and satellite-derived bathymetry.

It has been demonstrated that the sea surface gravity anomalies, derived from satellites observing variations in ocean surface height relative to the reference ellipsoid, can be used to provide a general view of the shape of deep ocean basins [63]. The so-called satellite altimetry-derived bathymetry is a source of absolute bathymetric information with global coverage and

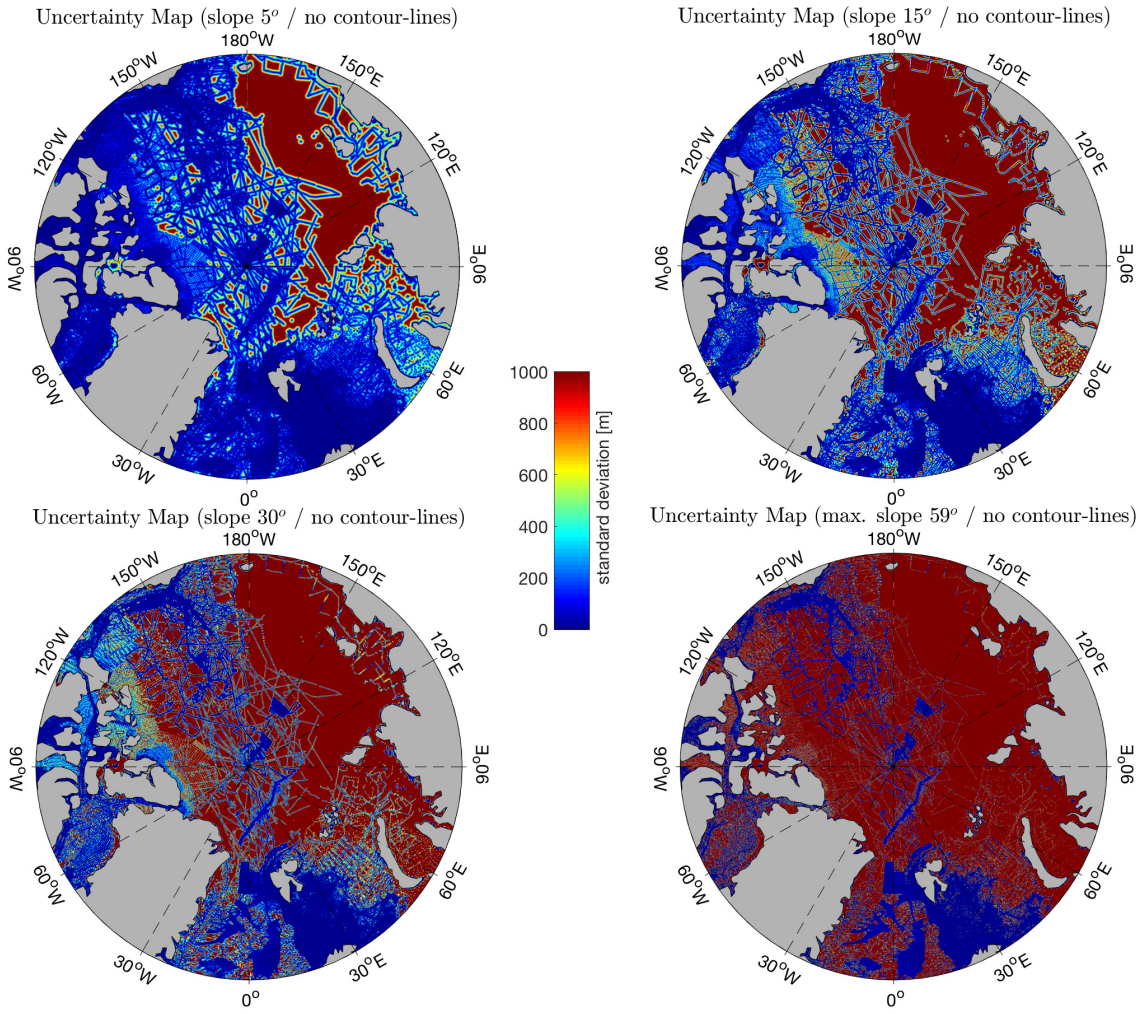

Fig. 6. Bathymetric uncertainty grid map computed for several values of the terrain slope when treating grid cells values based on bathymetric contour lines and other bathymetric models as if they were derived by interpolation.

can be used to coarsely fill gaps between sparse bathymetric measurements. Gravity anomalies measured over the Arctic Ocean can be correlated with the seafloor topography to provide a bathymetric evaluation in inaccessible areas. As such, gravity data has been used in IBCAO compilation process to check for potentially unmapped features or large offsets specifically in regions with sparse bathymetric data [64]. Therefore, it is unrealistic to expect massive vertical uncertainties, similar to those shown in Fig. 6, and thus an upper bound can be place. Here, it is assumed that the depth error cannot exceed 20% of the depth value of each grid cell. Although the resulting uncertainty potentially captures all errors in the IBCAO map, the upper bound of 40% of the depth is also considered as a worst-case scenario. Fig. 7 compares the two resulting

bathymetric uncertainty grid maps, which are generated by propagating errors proportionally to the extreme 59° terrain slope (hence forming the worst possible scenario for the IBCAO map).

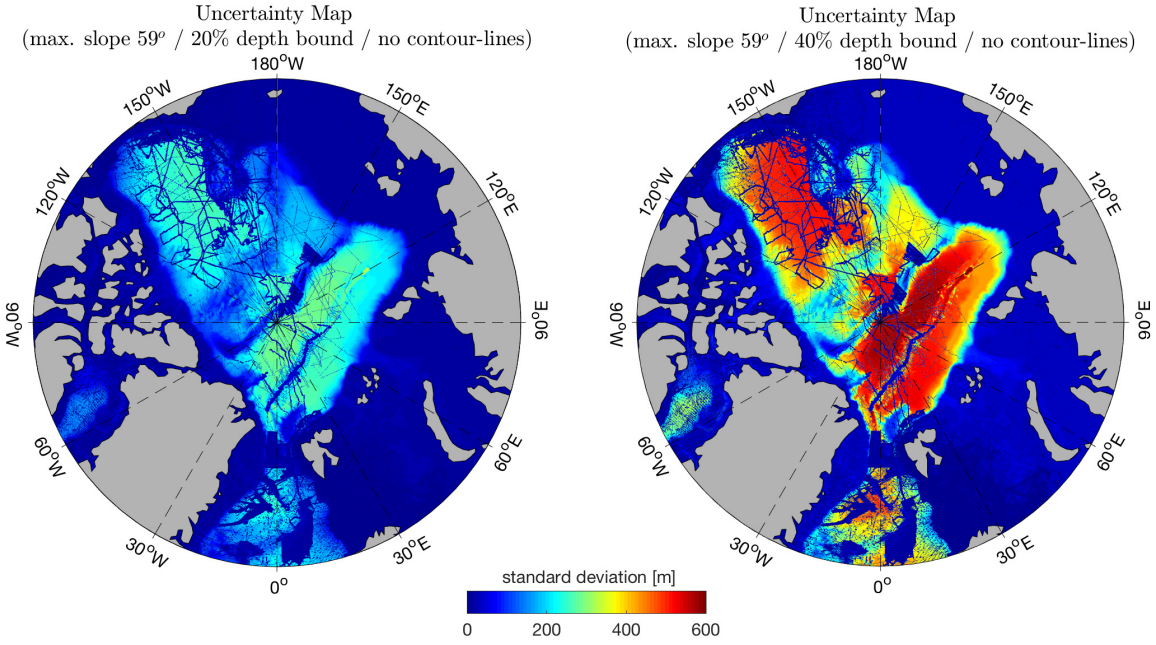

Fig. 7. Comparison between the resulting bathymetric uncertainty grid maps when placing a vertical error bound at 20% or at 40% of depth of each grid cell. Both grids are computed using 59° terrain slope and treating grid cells based on bathymetric contour lines and other bathymetric models as if they were grid cells subject to interpolation.

D. Distorting the Arctic Bathymetric Map

To evaluate the performance of the TAN algorithm under realistic conditions, it is assumed that the true terrain of the Arctic Ocean, $\bar{h}(\boldsymbol{x})$, is represented by the original IBCAO map, which remains unknown to the AUV during the simulated crossing. Instead, what is known to the vehicle is a terrain model, $h(\boldsymbol{x})$, which is created by distorting the true terrain map according to the developed bathymetric uncertainty model using the following expression:

$$h(\boldsymbol{x}) = \bar{h}(\boldsymbol{x}) + m(\boldsymbol{x}), \tag{9}$$

where the error $m(\boldsymbol{x})$ for each grid cell is sampled from $\mathcal{N}\big(0, \sigma_m^2(\boldsymbol{x})\big)$ and $\sigma_m(\boldsymbol{x})$ is defined by (8). After applying the error to each grid cell, the resulting $h(\boldsymbol{x})$ passes through a 2D Gaussian smoothing filter to remove high discontinuities, a common practice when generating bathymetric maps [47].

E. Likelihood Function Design

As discussed in section III-B, the noise in bathymetric observations can be modelled as $\mathcal{N}(0, \sigma^2_{\omega_k})$. Exploiting the error independence in the sensors involved, σ_{ω_k} can be computed by:

$$\begin{aligned}\sigma^2_{\omega_k} &= \sigma^2_s(r_k) + \sigma^2_d(d_k) = (K_1 \cdot r_k)^2 + (K_2 \cdot d_k)^2 \\ &= (3.3 \times 10^{-3} \cdot r_k)^2 + (10^{-2} \cdot d_k)^2,\end{aligned} \tag{10}$$

where $\sigma_s(r_k)$ corresponds to the error standard deviation in the measured range and $\sigma_d(d_k)$ represents the uncertainty in the derived operating depth, both varying proportionally to the measured quantity [34]. The constants K_1 and K_2 in (10) are defined empirically using field data collected from past experiments using these sensors. The maximum expected error in the vehicle's depth is approximately 0.1% of d_k ($K_1 = 3.3 \times 10^{-3}$ using the 3-σ rule of thumb), while preliminary analysis using data collected from recent deep water ($\approx$ 3000 m) experiments in the Celtic Sea (June 2018) suggest that the echo-sounder error can be approximately up to 3% of the measured range.

For the bathymetric map, the uncertainty model of the Arctic Ocean given in (8) is utilised. The RBPF algorithm uses $h(\boldsymbol{x})$ to calculate the water depth at each particle location, whist $\bar{h}(\boldsymbol{x})$ is used to generate bathymetric observations along the true vehicle path, which are then corrupted by sensor noise samples from $\mathcal{N}(0, \sigma^2_{\omega_k})$.

The weight of each of the N considered particles, $\{\boldsymbol{x}^i_k,\ i = 1, ..., N\}$, is computed using the following likelihood function:

$$p(z_k|\boldsymbol{x}^i_k) = \alpha \cdot exp\Big(-\frac{1}{2\sigma_{z_k}}\big(z_k - h(\boldsymbol{x}^i_k)\big)^2\Big), \tag{11}$$

where α is a normalisation constant and σ_{z_k}, based on (4), given as:

$$\sigma_{z_k} = \sqrt{\sigma^2_{\omega_k} + \max\Big\{\sigma^2_m(\boldsymbol{x}^1_k), ..., \sigma^2_m(\boldsymbol{x}^N_k)\Big\}}, \tag{12}$$

where the maximum $\sigma_m(\boldsymbol{x})$ among all particles is used to form the likelihood function. By selecting the maximum standard deviation to weight all particles, the RBPF algorithm adopts a conservative behaviour dependent on how reliable is the entire region where particles are spread out. In the event of traversing regions poorly mapped, this conservative setup will results in little trust on bathymetric observations and the filter will mostly perform time updates (particle time propagation). For a detailed description of the navigation filter, including mathematical formulation and parameters setup, readers are referred to [34], [37].

IV. Simulation Details

To evaluate the AUV navigation under the degraded performance of the heading sensors at high latitudes and the influence of the water currents, a simulated environment of the Arctic is developed in this section.

A. Arctic Water Circulation

To simulate the navigation drift caused by the water flow in the Arctic whilst operating mid-water column (i.e. far out of the ADCP's bottom-tracking range), the simulator is integrated with the NEMO model of the water circulation in the Arctic. Among other oceanographic parameters, NEMO provides a 3D grid of the water currents parametrised by location, depth and time. The spatial resolution of 0.083° in latitude and longitude is selected, which corresponds to the highest available resolution. Fig. 8 shows a random spatio-temporal instance of the water currents in the Arctic Ocean provided by the NEMO model at several depths. It can be inferred from this figure that currents weaken with depth.

To simulate therefore an ADCP providing water-relative velocity, the true (demanded) velocity vector is offset by the water current vector provided by the NEMO model at the true position of the vehicle (after first scaling the current vector by a factor of two to capture cases where the model may underestimate the true water speed).

B. Error Models for Heading Estimation in the Arctic

To simulate the errors in both heading sensors, models capturing the key sensor-dependent error sources are incorporated in the simulator. These error models have been developed in previous research and can be found in [33], [34]. The error model for the Octans gyrocompass incorporates error sources dependent on the operating latitude (distance from the Geographic North Pole) and the positioning error in latitude. This model was developed in conjunction with the sensor manufacturer and suggests that satisfactory performance can be obtained up to 88° latitude [53]. Therefore, the route shown in Fig. 3 keeps the minimum distance from the Geographic North Pole over 550 km (corresponding to an operational latitude below 85°). For the magnetic compass, the error model has an identical form, however the error terms in the model are significantly scaled causing larger errors as the position error increases and as approaching sensor-dependent critical regions (Magnetic North Pole). Therefore, the path shown

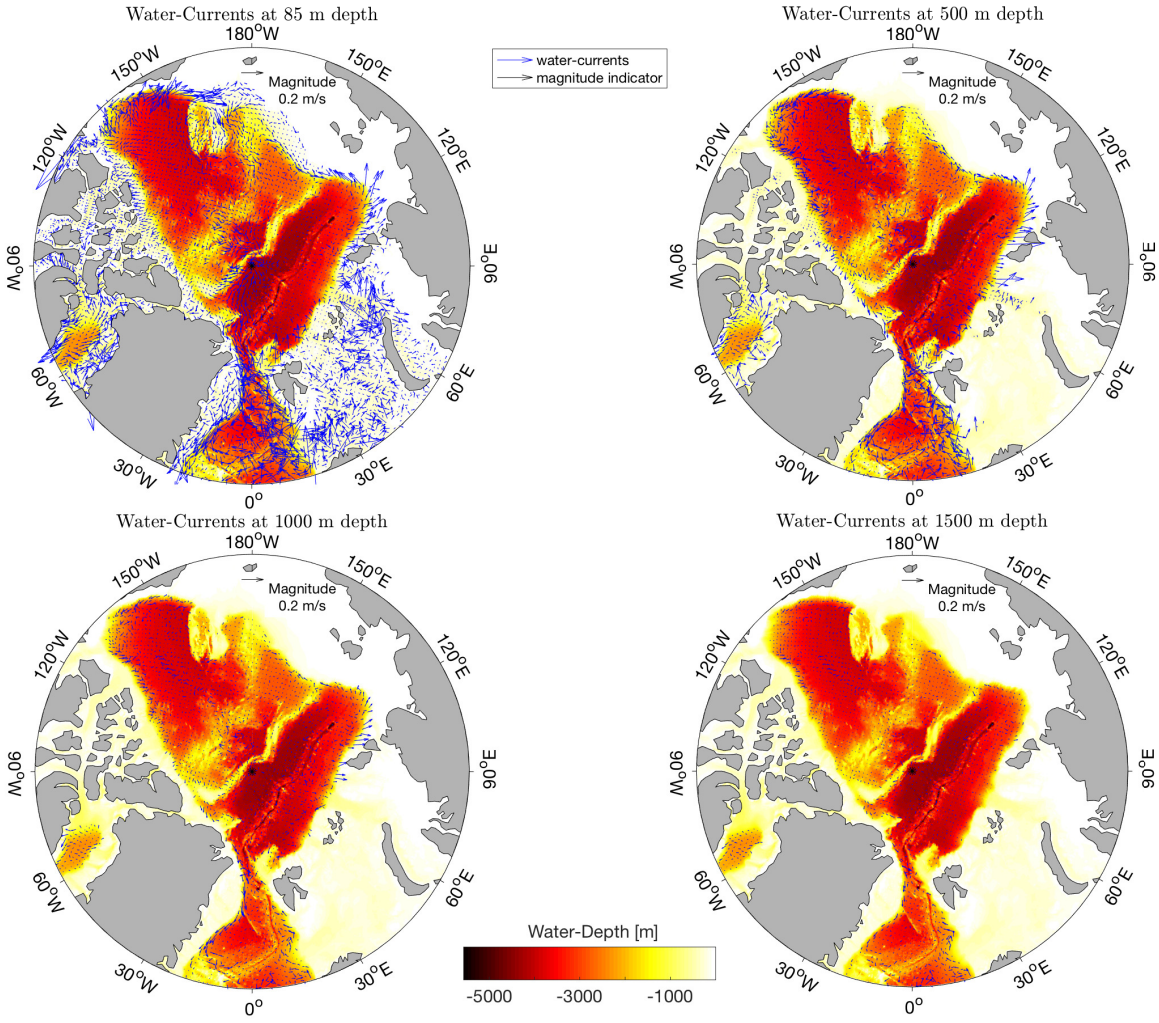

Fig. 8. A spatio-temporal instance of the water currents in the Arctic Ocean obtained from the NEMO model with respect to several depth layers (85 m, 500 m, 1000 m, and 1500 m).

in Fig. 3 approach as close as approximately 500 km to the Magnetic North Pole, whilst trying to avoid the flat terrain of the Canada Basin.

To apply heading errors in simulation, the true heading is deviated by the $3\times$ RMSE computed by the heading error model (effectively computing the maximum expected error by the three-σ rule of thumb). By applying heading errors this way, heading measurements are constantly biased towards a certain direction (east or west) during the entire mission. Although this may significantly overestimate the true error governing the heading sensors in the Arctic, it most importantly simulates the worst case scenario. Furthermore, a stochastic term (Gaussian noise) is also added to each heading measurement to represent potentially unmodelled noises, e.g.

variations in the magnetic field because of crustal anomalies and solar storms (although these would probably be better described by an error impulse—with a tail over minutes or hours—with Poisson occurrence distribution).

V. Crossing the Arctic Ocean with ALR1500 and Terrain-Aided Navigation

Using the simulated environment developed previously, this section evaluates the performance of the TAN algorithm with respect to several factors, such as the vertical bathymetric uncertainty in the IBCAO grid map. By varying the value of the maximum considered terrain slope (s_{max}) and the upper bathymetric uncertainty bound, five different configurations of the bathymetric uncertainty grid map are considered:

- $s_{max} = 5^\circ$ and uncertainty bound at 20% of depth (*config.1*);
- $s_{max} = 5^\circ$ and uncertainty bound at 40% of depth (*config.2*);
- $s_{max} = 15^\circ$ and uncertainty bound at 40% of depth (*config.3*);
- $s_{max} = 30^\circ$ and uncertainty bound at 40% of depth (*config.4*);
- $s_{max} = 59^\circ$ (calculated maximum) and uncertainty bound at 40% of depth (*config.5*).

A set of R = 10 experiments (crossing repetitions) is performed for each configuration of bathymetric uncertainty grid map. Each simulation run generates a new terrain model $h(\boldsymbol{x})$ using (9). The navigation algorithm is evaluated in terms of position accuracy and estimation uncertainty (refer to Table I for the summary of the key simulation parameters and performance measures). Initial experiments assume that ALR1500 uses a magnetic compass for heading estimation. If the navigation error exceeds the maximum acceptable error (100 km), it will be assumed that TAN has failed. In such an event, new simulation runs will be performed using the Octans gyrocompass for heading determination.

Table II summarizes the simulation results using suitable performance measures described in Table I (refer to Salavasidis, *et al.* [38] for definitions). No divergence is recorded for the first three configurations of the bathymetric uncertainty grid map. For the least uncertain configuration (*config.1*), the maximum instantaneous error (max. RMSE) among all simulation runs is 30 km, while the error averaged over mission length and all 10 simulation runs ($RMSE^{10}$) is just under 2 km. For *config.2*, the $RMSE^{10}$ grows to 4 km whilst the maximum instantaneous error among all simulation runs increases to 71 km. Surprisingly, the maximum instantaneous error for *config.2* is double than the same error for *config.3*, although in the latter scenario the bathymetric uncertainty grid map is constructed using a higher value for the maximum terrain slope. One

TABLE I

SIMULATION PARAMETERS & PERFORMANCE MEASURES

number of simulation runs	R = 10 (20 in section VI)
number of particles	N = 1000
position propagation period	Δt = 1 sec
forward speed	0.6 m/s
operating depth	1000 m (min. distance from bottom 100 m)
sonar measur. repetition rate	60 sec
$RMSE^R$	RMSE averaged over time and R simulation runs
$RMSE_k^R$	RMSE at time k averaged over R simulation runs
max. RMSE	maximum instantaneous RMSE among R simulation runs

potential explanation could be the relatively small number of simulation runs, which causes this discrepancy in the maximum instantaneous error.

TABLE II

TAN PERFORMANCE WHEN USING MAGNETIC COMPASS

-	$RMSE^{10}$	max. RMSE	Divergence
config.1	2 km	30 km	0
config.2	4 km	71 km	0
config.3	4 km	36 km	0
config.4	4 km	69 km	1
config.5	4 km	40 km	2

TAN performance measures calculated over 10 simulated crossings of the Arctic for each considered configuration of the bathymetric uncertainty model when using a magnetic compass for heading estimation. Unsuccessful runs (filter divergence) are excluded from the calculations.

The first three sets of experiences are considered successful as the maximum instantaneous error among all simulation runs is under 100 km. Furthermore, Fig. 9 shows the averaged time-indexed error ($RMSE_k^{10}$), which is the RMSE at k averaged over the all 10 simulation runs, and the 3-σ confidence bounds[3] for *config.2* and *config.3* experiments. It is clear that the navigation

[3]The uncertainty in position is visualised as if the particles were always distributed following a bi-variate normal distribution uncorrelated in latitude and longitude, although this assumption may occasionally be invalid (when the state posterior probability density function is highly multimodal) [37].

filter never underestimates the error in position as the latter always falls within the uncertainty bounds.

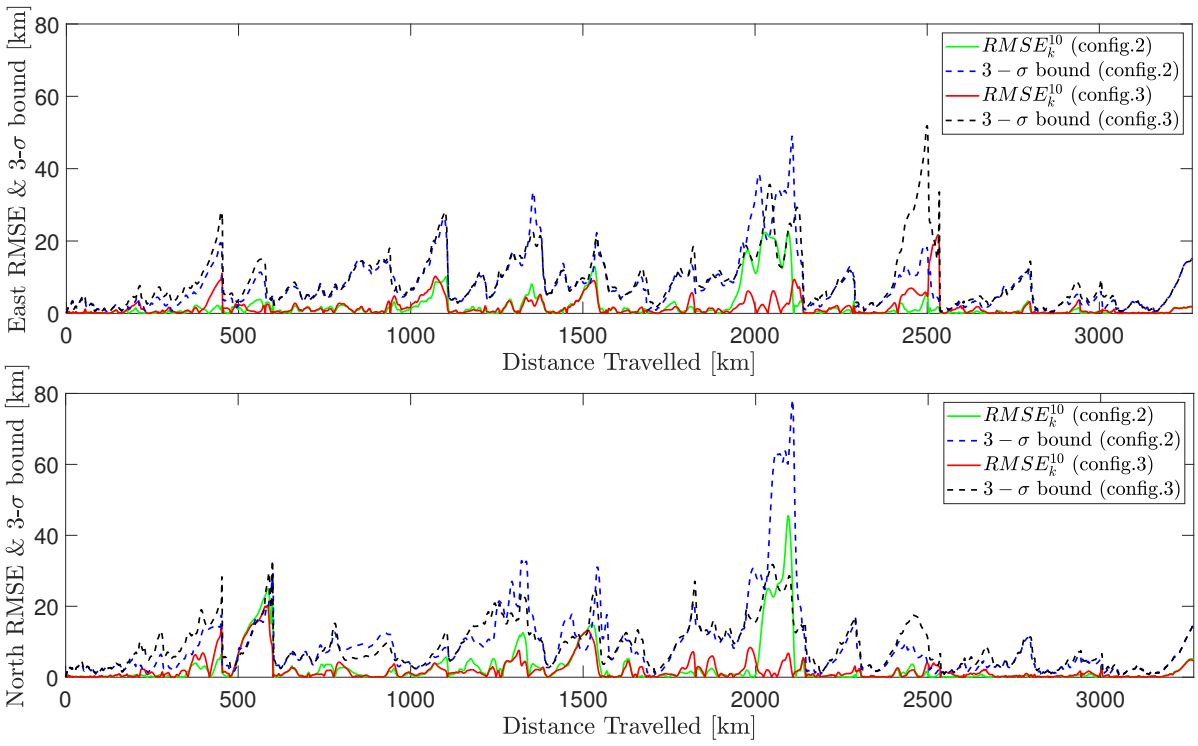

Fig. 9. Navigation error with the corresponding 3-σ bound in the north and east direction over distance travelled for *config.2* and *config.3*. Quantities averaged over 10 simulation runs when using a magnetic compass for heading estimation.

Notice also that in the majority of the mission the TAN performance appears to be similar for both experiments, except two distinct instances at approximately 2000 km and 2500 km of DT. This is where the state posterior probability density function is temporarily bimodal (two peaks) causing the increase in the navigation error (as the point estimates fall between the two modes). Moreover, while the filter always converge to the true mode, the approximated bimodal state posterior density at 2000 km of DT for the *config.2* experiments is the reason for the—unexpectedly—higher error peak compared to the *config.3* experiments.

By distorting the bathymetric map further (*config.4* and *config.5*), one divergence for *config.4* and two divergences for *config.5* are recorded (note that the performance measures reported in Table II are calculated after excluding the unsuccessful runs). Therefore, particularly for these two configurations of the bathymetric uncertainty grid map a new set of 10 experiments is performed whilst using the Octans gyrocompass for heading estimation. Table III summarises

the navigation results.

TABLE III
TAN PERFORMANCE WHEN USING GYROCOMPASS

-	$RMSE^{10}$	max. RMSE	Divergence
config.4	4 km	91 km	2
config.5	3 km	39 km	2

TAN performance measures calculated over 10 simulated crossings of the Arctic when using the Octans gyrocompass for heading estimation. Unsuccessful runs (filter divergence) are excluded from the calculations.

Despite using the gyrocompass, the TAN algorithm appears to be unable to provide a reliable navigation solution as two divergences are recorded for each of the two configurations of the uncertainty grid map. To show the effect of the heading sensor on the TAN performance, Figs. 10 and 11 present the averaged time-indexed error ($RMSE_k^{10}$) with the associated estimation uncertainty for each heading sensor for the *config.4* and *config.5* experiments, respectively.

In the majority of the mission length, the TAN algorithm exhibits similar performance for both heading sensors. This implies that the map errors together with the terrain morphology are the key factors driving the estimation accuracy of TAN. The performance of the RBPF algorithm appears to be significantly decreased in three distinguishable instances, marked as A, B, and C in Figs. 10 and 11. Moreover, Fig. 12 shows the exact location of these three instances on the bathymetric uncertainty grid map for *config.5*, together with the path estimated by the TAN algorithm (averaged over the successful runs) when using the gyrocompass. Two out of all three recorded divergences occurred in C when using a magnetic compass, whereas using the gyrocompass three out of all four divergences occurred in B. Also, a single divergence was recorded in A for both heading sensor as ALR1500 traverses a large region with high bathymetric uncertainty.

Fig. 13 shown the behaviour of the particle filter at these three particular instances. The left-hand side plots, which are marked with a minus superscript, show the causes driving the navigation filter to a degraded performance (or even to a divergence), whereas the right-hand side plots with a plus superscript refer to the time instance after which the filter recovers and converges to the true position (thus the figure represents only successful runs). Plots corresponding to the instance A (A^- and A^+) show the vehicle traversing a large region with high bathymetric

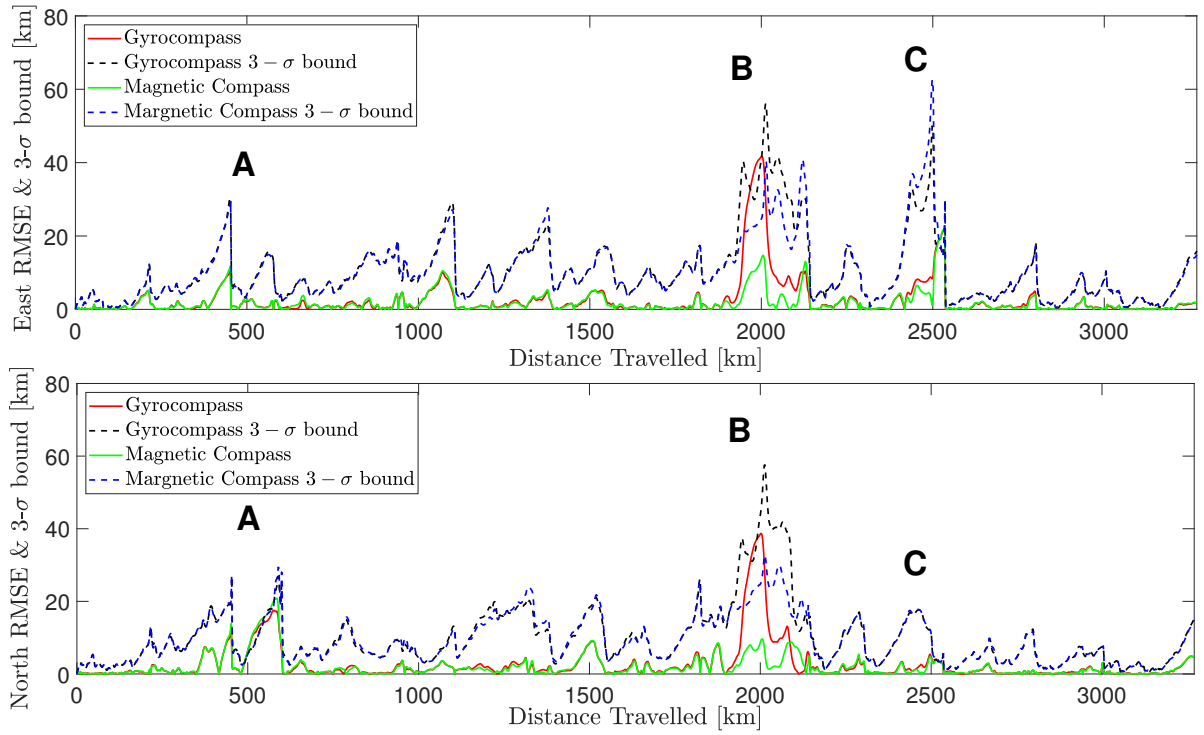

Fig. 10. Navigation error with the corresponding 3-σ bound in the north and east direction over distance travelled for *config.4*. Quantities averaged over the successful simulation runs when using either a magnetic compass or the Octans gyrocompass for heading estimation.

uncertainty. Therefore, as the likelihood function flatten to avoid using unreliable bathymetric features, the navigation filter is unable to compensate for the drift caused by the errors in the motion sensors. This made the filter to diverge one time for each heading sensor for the most uncertain configuration of the bathymetric map (*config.5*). The rest divergences occurred in B and in C. Closer examination at these particularly locations revealed that the presence of multiple local minima whilst traversing regions with high bathymetric uncertainty cause the navigation filter to approximate a multi-modal state posterior probability density function (e.g. see instance B^- in Fig. 13) . As a result, in five occasions (for both heading sensors) the filter eventually performed false convergence without the ability to recover.

The conjecture that map errors primarily drive the TAN performance can be verified by observing Fig. 14. This figure shows an example of the vertical distortion applied to each grid cell of the "true" Arctic bathymetric map $\bar{h}(\boldsymbol{x})$ along the true path of the vehicle in order to create $h(\boldsymbol{x})$, which is subsequently utilised by the TAN algorithm. It appears that the map

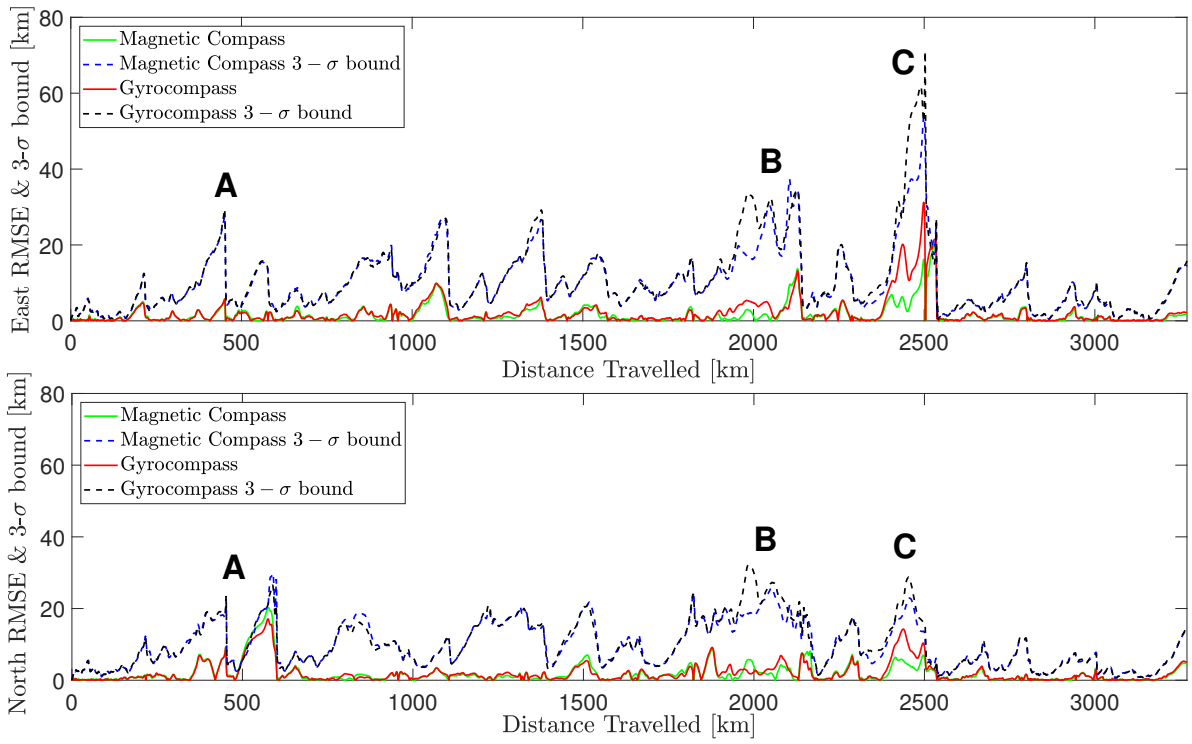

Fig. 11. Navigation error with the corresponding 3-σ bound in the north and east direction over distance travelled for *config.5*. Quantities averaged over the successful simulation runs when using either a magnetic compass or the Octans gyrocompass for heading estimation.

errors are at the highest level in the three instances (A, B, and C) where TAN experienced difficulties to estimate reliably the vehicle's position. Notice also that map errors for *config.4* and *config.5* experiments can sometimes be comparable, despite that the value of the maximum terrain slope used for the *config.5* experiments is almost double than the one used for the *config.4* experiments. However, when saturating/bounding the map uncertainty based on the depth value (see Section III-C2), identical standard deviations may eventually be obtained. Therefore, the effect of using high s_{max} is primarily noticeable in the deep part of the ocean (e.g. see Fig. 14 at approximately 200-500 km and 1800-2500 km of DT).

VI. Improving TAN Performance via Path-Planning

It was postulated in the previous section that the TAN performance can be improved by avoiding traversing large regions with high bathymetric uncertainty. This concept has already been exploited by generating tracks along areas with rich topographic information [65]–[67]. However, the results in Section V show that it is not sufficient only to avoid traversing featureless

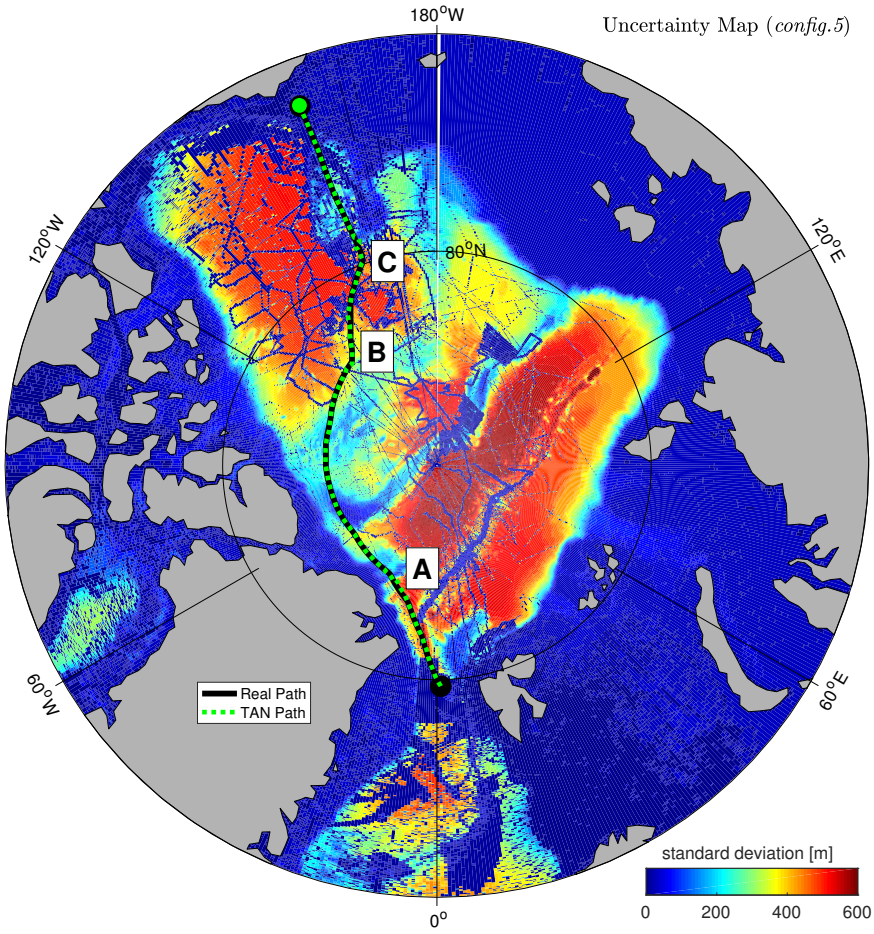

Fig. 12. The true AUV path and the one estimated by the TAN algorithm (averaged over the successful runs) for *config.5* when using the Octans gyrocompass. Three locations, marked with A, B and C, where the filter experienced at least a single divergence among all simulation runs, either when using a magnetic compass or the gyrocompass.

terrains, such as the Canada Basin [49], when using coarse bathymetric maps. In addition to the terrain morphology, the bathymetric uncertainty must be considered.

Therefore, a new path for the ALR1500 is designed using an RRT* algorithm [48], which is specifically developed for the Arctic crossing experiments using the IBCAO bathymetric map and corresponding bathymetric uncertainty model given in (8), as well as the motion and sensor characteristics of the ALR1500. The path is optimised primarily to abstain large regions with high bathymetric uncertainty and secondarily to avoid traversing low-informative terrains, keeping distance from heading sensor-dependent critical zones, and minimising the total mission length. However, these are all parameters of the cost function used by the RRT* algorithm and can be re-weighted according to the needs. Further details about this algorithm will not be provided

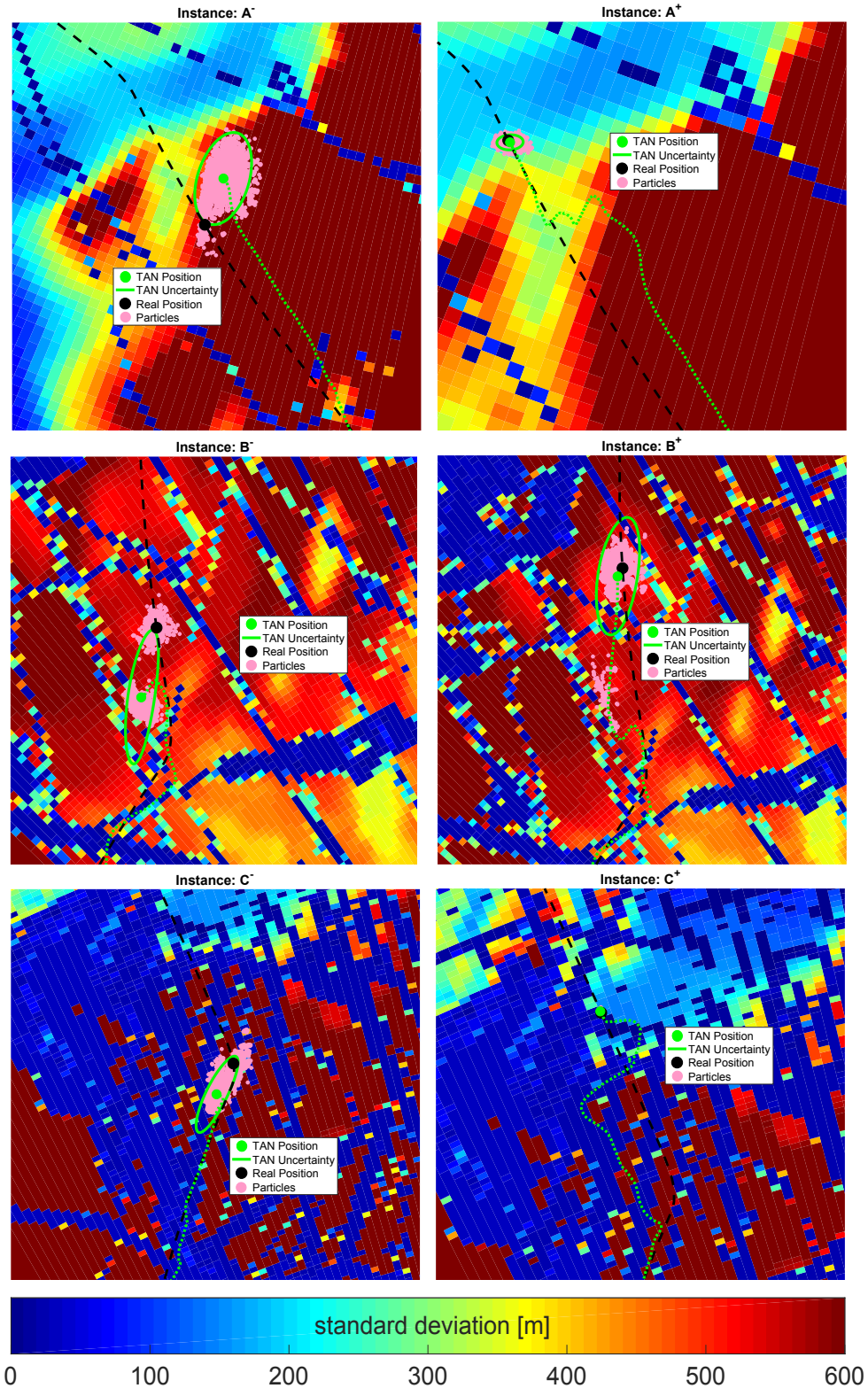

Fig. 13. The behaviour of the RBPF algorithm at locations where TAN experienced reduced performance (or even estimation divergence). Plots marked with a minus superscript (left-hand side) show the causes for the filter's low performance. Plots with a plus superscript (right-hand side) refer to the time-instance during successful simulation runs where the filter eventually recovers and convergences to the true position (in C^+ plot all particles are under the true vehicle position).

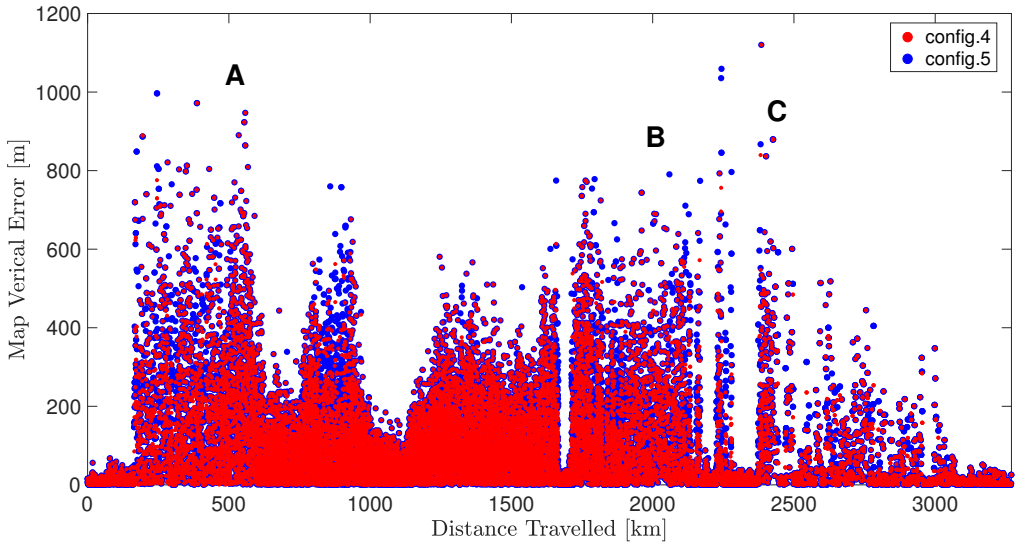

Fig. 14. An example of the vertical map error (distortion) applied to the "true" Arctic bathymetric map along the true path of the vehicle for *config.4* and *config.5*.

here, as the general path-planning concept is out of the scope of this work.

Fig. 15 presents the optimised path. Two insets to this figure show that the new path tries to bypass extended regions with high bathymetric uncertainty by guiding the vehicle towards grid cells for which the depth values are primarily computed using sonar data (e.g. following potential ship track-lines). Also, Fig. 16 compares the vertical bathymetric uncertainty along the initial path and the optimised one. It is worth to highlight that the new path is by no means an optimal one, but rather an output example of the RRT* algorithm based on the optimisation criteria discussed previously. Because of this optimisation setup, the new path inevitably approaches closer to the Magnetic North Pole and the total mission range increases to approximately 3700 km (although range reduction can still be made given that the mission begins in open ocean far from areas expected to be covered by ice).

Using the optimised path, a new set of $R = 20$ crossing repetitions is performed for *config.5* and each heading sensor. Simulation results are summarised in Table IV.

No filter divergence is recorded during the new experiments, regardless which heading sensor is used. Furthermore, the performance measures calculated show that the use of the gyrocompass improves the TAN estimation accuracy. However, the most important observation is that the navigation filter does not experience high error peaks, as it does for the experiments using the

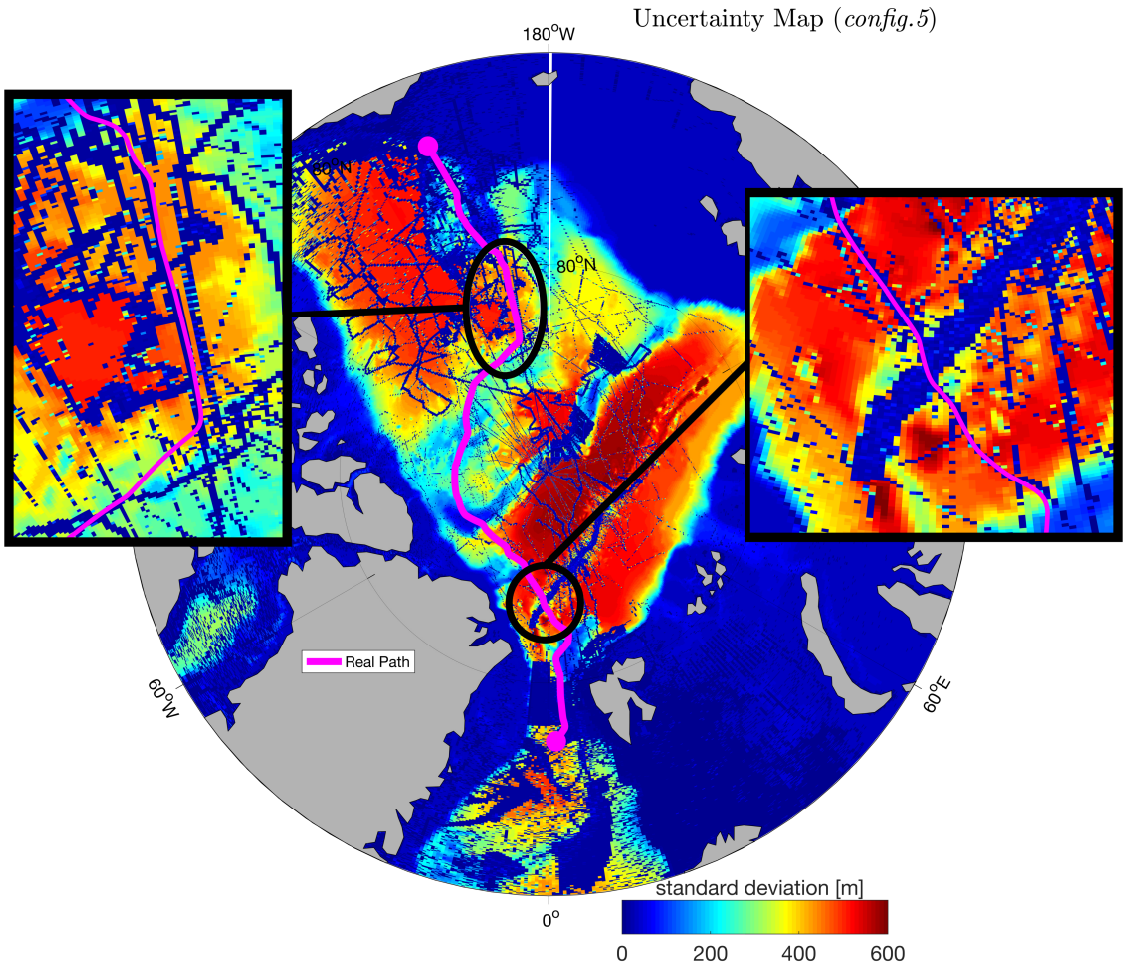

Fig. 15. An optimised path for crossing the Arctic using TAN. The path is generated by an RRT* algorithm configured primarily to abstain large regions with high bathymetric uncertainty.

TABLE IV

TAN PERFORMANCE GIVEN AN OPTIMISED PATH

-	Magnetic Compass		Gyrocompass	
	DR	TAN	DR	TAN
$RMSE^{20}$	792 km	4 km	181 km	3 km
max. RMSE	2958 km	28 km	605 km	27 km
Divergence	-	0	-	0

TAN performance measures calculated over 20 simulated crossings of the Arctic for *config.5* whilst using either a magnetic compass or the Octans gyrocompass for heading estimation. The true AUV path is optimised using the RRT* algorithm.

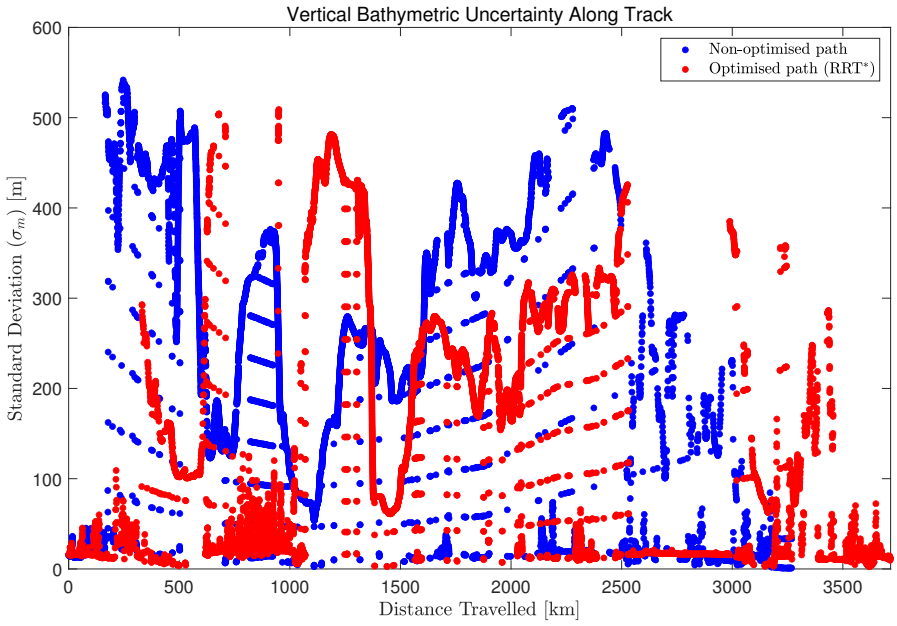

Fig. 16. Vertical bathymetric uncertainty along the initial path (non-optimised) and the path computed using the RRT* optimisation algorithm.

non-optimised path. The error averaged over mission length and all 20 simulation runs, $RMSE^{20}$, is 3 km when using the gyrocompass and 4 km when using the magnetic compass, whist the error peaks (max. RMSE) among all simulation runs are 27 km and 28 km for the gyrocompass and magnetic compass, respectively.

Fig. 17 shows the averaged time-indexed error $RMSE_k^{20}$ and the associated uncertainty for both heading sensors. It appears that the filter is relatively uncertainty at 2700 km of DT, however this does not result in high estimation error as the state posterior density function remains approximately unimodal. The estimated average path of the vehicle for each heading sensor is visualised in Fig. 18. As expected, the DR navigation experiences large positioning error at the end of the mission. This is mainly due to the errors in heading, as they are modelled in a way to provide an estimate of the upper error bound for the DR navigation (hence the extreme DR error).

VII. Conclusion and Future Work

Many of the current challenges in ocean science focus on biogeochemical processes taking place in remote and hazardous environments. While long-range AUVs have been developed

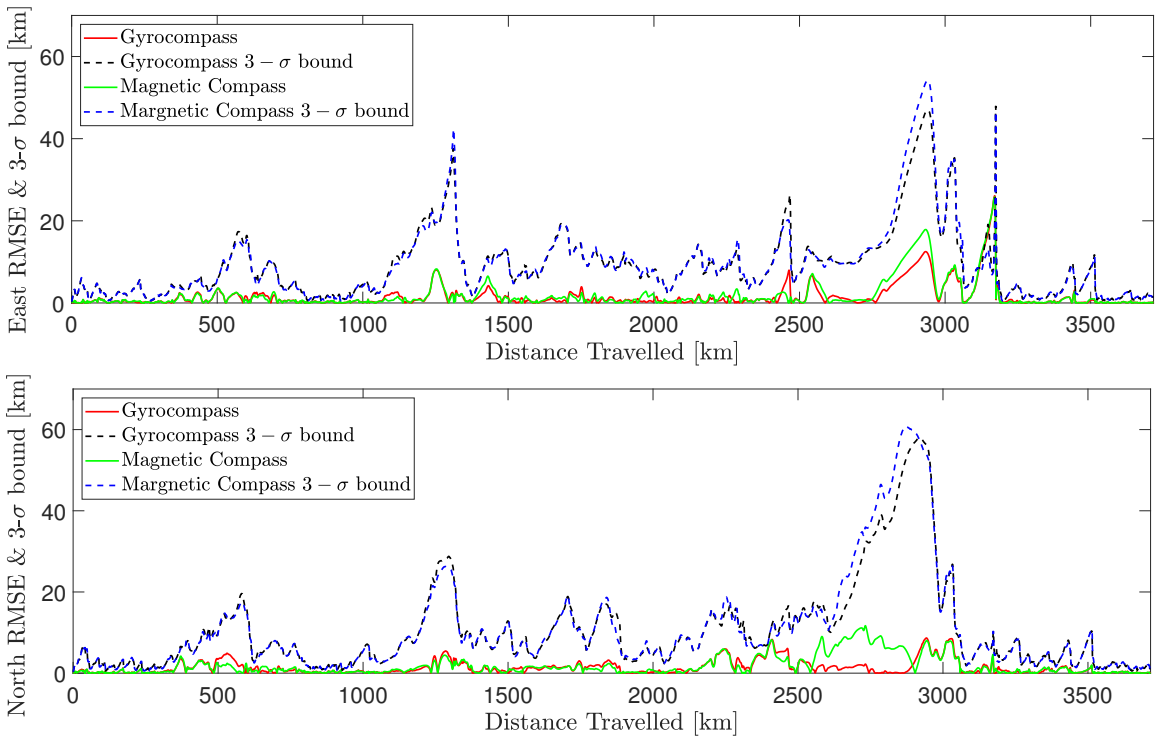

Fig. 17. Navigation error with the corresponding 3-σ bound in the north and east direction over distance travelled for *config.5* when optimising the true AUV path using the RRT* algorithm. Quantities averaged over 20 simulation runs when using either a magnetic compass or the Octans gyrocompass for heading estimation.

offering unparalleled opportunities for multi-month continuous data-collection in previously inaccessible areas, the presently weak underwater navigation challenges the feasibility of undertaking missions of the order of months in GPS-denied environments.

In response, this work examines whether TAN techniques can be used to prolong underwater missions, without the need for external support or regular surfacing, whilst relying on a small number of low-power sensors and sparse bathymetric maps. In particular, the ALR1500 was assumed to undertake a science-driven mission of a continuous mid-water survey from Svalbard to Point Barrow under the Arctic sea ice—a range in excess of 3200 km. To evaluate the navigation performance, a simulated environment of the Arctic Ocean was developed which integrates error models for heading estimation at high latitudes, a state-of-the-art model of ocean circulation, and the Arctic bathymetry.

To take into consideration that large areas in the bathymetric map of the Arctic Ocean are subjected to interpolation, a bathymetric uncertainty grid map was developed which assigns a

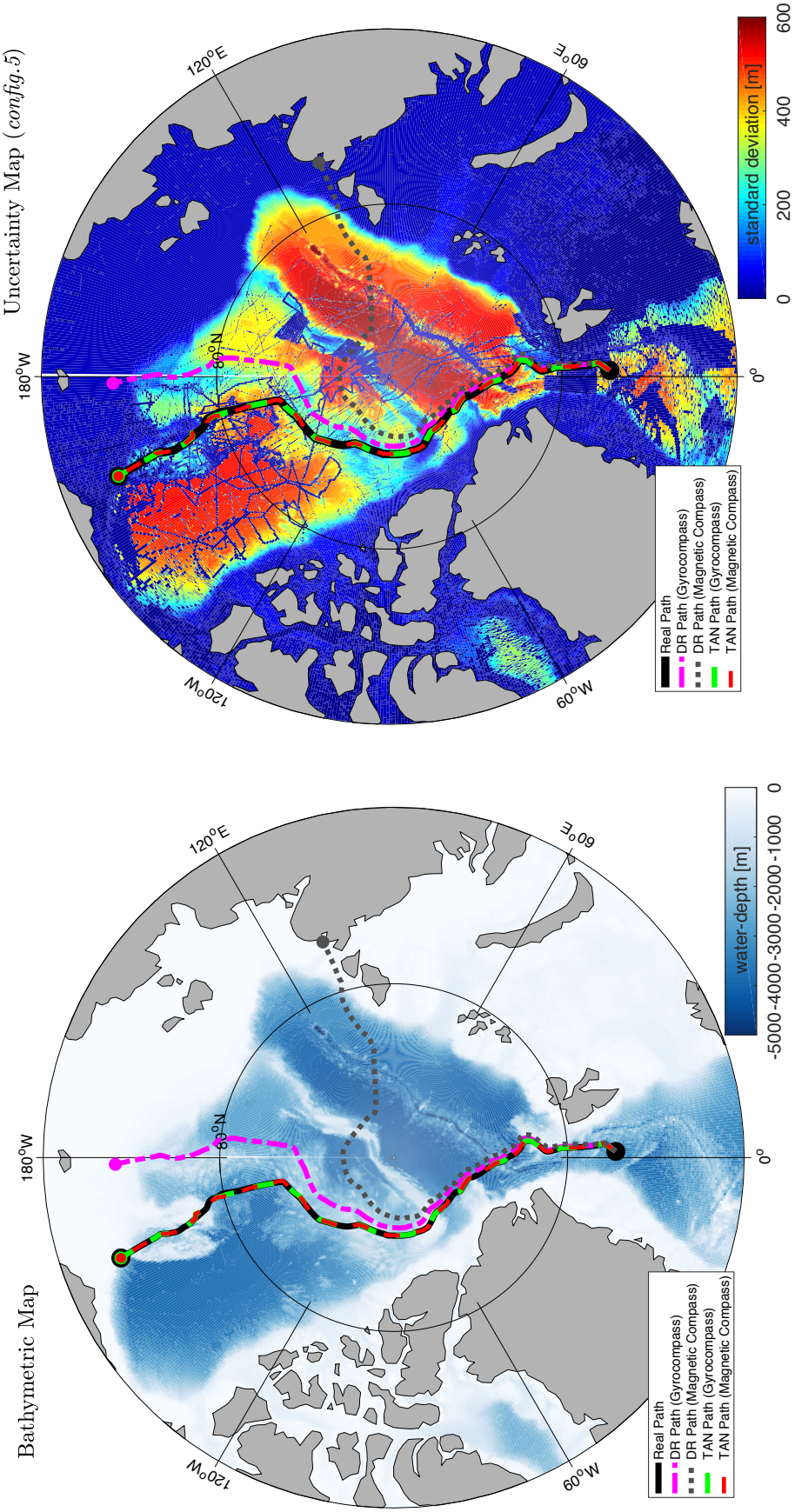

Fig. 18. DR and TAN results when crossing the Arctic Ocean. For heading estimation, either a magnetic compass or the Octans gyrocompass is used. The true AUV path is optimised by using an RRT* algorithm to primarily avoid traversing large regions with high bathymetric uncertainty.

638 degree of reliance to each grid cells of the bathymetric map. The uncertainty for depth values
639 derived from sonar measurements was calculated using statistics reported from historical deep
640 water sonar measurements. For grid cells subject to interpolation, uncertainties were calculated
641 proportionally to the cell's distance from the closest reliable grid cell (i.e. a cell with depth value
642 derived from sonar measurements). This uncertainty model effectively penalises regions where
643 the map is constructed using interpolation.

644 To obtain bathymetric observations in the deep Arctic, the NOC's 4000 m range single-beam
645 echo-sounder was configured at one-minute pinging period (for maximum energy conservation)
646 and used. The performance of the TAN algorithm was examined with respect to the employed
647 heading sensor and a range of vertical distortions applied to the reference map, which were
648 calculated according to the bathymetric uncertainty model developed for the Arctic bathymetric
649 map. This effectively simulates the bathymetric conditions that the TAN algorithm is likely to
650 be facing when using coarse bathymetric maps.

651 Using the simulated environment of the Arctic, an unaided navigation solution inevitably
652 experienced an error of hundreds of kilometres which is, however, dependent on the employed
653 heading sensor, whereas TAN provided acceptable positioning accuracy given a moderate map
654 distortion. By degrading the quality of the bathymetric map further, it appears that TAN can fail
655 when operating in large areas with high bathymetric uncertainty. Therefore, an RRT* algorithm
656 was used to design a new path such that the AUV traverses reliable and rich in topographic
657 information regions. Numerical experiments show that using the optimised AUV path it is
658 possible to enable safe transit, despite heavily distorting the reference map.

659 Future work will focus on further improving the NOC's navigation system by integrating other
660 geophysical quantities (e.g. geomagnetic [54] and gravity information [68]) and/or oceanographic
661 parameters [69] as navigation references. Furthermore, a future aim is to uses the heading sensors
662 in combination. For example, the gyrocompass can be used as a reference to correct the magnetic
663 compass for short periods of time, or can be switched off for energy conservation when the
664 magnetic compass is reliable enough. The deviation between the heading sensors may also turn,
665 in certain circumstances, into a useful navigational source of information relative to magnetic
666 declination maps. A future goal is also to develop terrain uncertainty models that takes into
667 account terrain dependencies, as well as investigating the feasibility of using more complex
668 interpolation techniques in real-time (e.g. instead of using bi-linear interpolation [38]). Towards
669 this direction, geostatistical models may turn to be very useful (e.g. Kriging methods that use

variogram models and Gaussian process models).

ACKNOWLEDGMENT

This work was supported by the ROBOCADEMY (FP7 Marie Curie Programme ITN Grant Agreement Number 608096) and NERC Oceanids programme. The authors would like to thank Dr Stephen Kelly for assisting in obtaining the NEMO data, Dr Yanqing Jiang for his contribution in developing the path planning algorithm, Dr Povl Abrahamsen for kindly providing the bathymetric data used in Fig. 1 and the MARS engineers in developing ALR1500.

REFERENCES

[1] P. Wassmann, C. M. Duarte, S. Agusti, and M. K. Sejr, "Footprints of Climate Change in the Arctic Marine Ecosystem," *Global change biology*, vol. 17, no. 2, pp. 1235–1249, 2011. doi: 10.1111/j.1365-2486.2010.02311.x

[2] M. C. Serreze and R. G. Barry, "Processes and impacts of arctic amplification: A research synthesis," *Global and planetary change*, vol. 77, no. 1-2, pp. 85–96, 2011. doi: 10. 1016/j.gloplacha.2011.03.004

[3] T. Jung, N. D. Gordon, P. Bauer, D. H. Bromwich, M. Chevallier, J. J. Day, J. Dawson, F. Doblas-Reyes, C. Fairall, H. F. Goessling *et al.*, "Advancing polar prediction capabilities on daily to seasonal time scales," *Bulletin of the American Meteorological Society*, vol. 97, no. 9, pp. 1631–1647, 2016. doi: 10.1175/BAMS-D-14- 00246.1

[4] G. C. Smith, R. Allard, M. Babin, L. Bertino, M. Chevallier, G. Corlett, J. Crout, F. Davidson, B. Delille, S. T. Gille *et al.*, "Polar ocean observations: A critical gap in the observing system and its effect on environmental predictions from hours to a season," *Frontiers in Marine Science*, vol. 6, p. 429, 2019. doi: 10.3389/fmars.2019.00429

[5] D. Lubin and R. Massom, *Polar Remote Sensing: Volume I: Atmosphere and Oceans*. Springer Science & Business Media, 2006.

[6] J. Calder, A. Proshutinsky, E. Carmack, I. Ashik, H. Loeng, J. Key, M. McCammon, H. Melling, D. Perovich, H. Eicken *et al.*, "An integrated international approach to Arctic Ocean observations for society (A legacy of the International Polar Year)," *Proceedings of OceanObs'09: Sustained Ocean Observations and Information for Sociaty*, vol. 9, 2010. doi: 10.5270/OceanObs09.cwp.14

[7] D. Roemmich and J. Gilson, "The 2004–2008 mean and annual cycle of temperature, salinity, and steric height in the global ocean from the Argo Program," *Progress in Oceanography*, vol. 82, no. 2, pp. 81–100, 2009. doi: 10.1016/j.pocean.2009.03.004

[8] S. L. Castro, G. A. Wick, and M. Steele, "Validation of satellite sea surface temperature analyses in the Beaufort Sea using UpTempO buoys," *Remote Sensing of Environment*, vol. 187, pp. 458–475, 2016. doi: 10.1016/j.rse.2016.10.035

[9] G. Johnsen, M. Norli, M. Moline, I. Robbins, C. von Quillfeldt, K. Sørensen, F. Cottier, and J. Berge, "The advective origin of an under-ice spring bloom in the Arctic Ocean using multiple observational platforms," *Polar biology*, vol. 41, no. 6, pp. 1197–1216, 2018. doi: 10.1007/s00300-018-2278-5

[10] C. Katlein, S. Arndt, M. Nicolaus, D. K. Perovich, M. V. Jakuba, S. Suman, S. Elliott, L. L. Whitcomb, C. J. McFarland, R. Gerdes *et al.*, "Influence of ice thickness and surface properties on light transmission through arctic sea ice," *Journal of Geophysical Research: Oceans*, vol. 120, no. 9, pp. 5932–5944, 2015.

[11] C. M. Lee, S. Cole, M. Doble, L. Freitag, P. Hwang, S. Jayne, M. Jeffries, R. Krishfield, T. Maksym, and W. Maslowski, "Marginal Ice Zone (MIZ) program: Science and experiment plan," Washington University, Applied Physics Lab, Seattle, Tech. Rep., 2012.

[12] D. Fissel, J. Marko, and H. Melling, "Advances in upward looking sonar technology for studying the processes of change in arctic ocean ice climate," *Journal of Operational Oceanography*, vol. 1, no. 1, pp. 9–18, 2008. doi: 10.1080/1755876X.2008.11081884

[13] S. McPhail, R. Templeton, M. Pebody, D. Roper, and R. Morrison, "Autosub long range auv missions under the filchner and ronne ice shelves in the weddell sea, antarctica-an engineering perspective," in *OCEANS–Marseille*. IEEE, 2019. doi: 10.1109/OCEANSE.2019.8867206 pp. 1–8.

[14] P. Norgren and R. Skjetne, "Using Autonomous Underwater Vehicles as Sensor Platforms for Ice-Monitoring," *Modeling, Identification and Control*, vol. 35, no. 4, pp. 263–277, 2014. doi: 10.4173/mic.2014.4.4

[15] P. Wadhams, J. P. Wilkinson, and S. McPhail, "A new view of the underside of arctic sea ice," *Geophysical Research Letters*, vol. 33, no. 4, 2006. doi: 10.1029/2005GL025131

[16] C. R. German, D. R. Yoerger, M. Jakuba, T. M. Shank, C. H. Langmuir, and K.-I. Nakamura, "Hydrothermal Exploration with the Autonomous Benthic Explorer," *Deep Sea Research Part I: Oceanographic Research Papers*, vol. 55, no. 2, pp. 203–219, 2008. doi: 10.1016/j.dsr.2007.11.004

[17] X. Xiang, B. Jouvencel, and O. Parodi, "Coordinated Formation Control of Multiple Autonomous Underwater Vehicles for Pipeline Inspection," *International Journal of Advanced Robotic Systems*, vol. 7, no. 1, p. 3, 2010.

[18] A. C. Kapoutsis, S. A. Chatzichristofis, L. Doitsidis, J. B. de Sousa, J. Pinto, J. Braga, and E. B. Kosmatopoulos, "Real-time Aadaptive Multi-Robot Exploration with Application to Underwater Map Construction," *Autonomous robots*, vol. 40, no. 6, pp. 987–1015, 2016. doi: 10.1007/s10514-015-9510-8

[19] V. Yordanova, B. Gips, T. Furfaro, and S. Dugelay, "Coverage path planning for mine countermeasures: Adapting track orientation," in *OCEANS–Marseille*. IEEE, 2019, pp. 1–7.

[20] C. Kaminski, T. Crees, J. Ferguson, A. Forrest, J. Williams, D. Hopkin, and G. Heard, "12 days under ice – an historic auv deployment in the canadian high arctic," in *2010 IEEE/OES Autonomous Underwater Vehicles*, 2010. doi: 10.1109/AUV.2010.5779651 pp. 1–11.

[21] L. D. L. Barker and L. L. Whitcomb, "A preliminary survey of underwater robotic vehicle design and navigation for under-ice operations," in *2016 IEEE/RSJ International Conference on Intelligent Robots and Systems (IROS)*. IEEE, 2016. doi: 10.1109/IROS.2016.7759319 pp. 2028–2035.

[22] P. Norgren, R. Lubbad, and R. Skjetne, "Unmanned underwater vehicles in Arctic operations," in *Proceedings of the 22nd IAHR International Symposium on Ice, Singapore*, 2014, pp. 89–101.

[23] R. McEwen, H. Thomas, D. Weber, and F. Psota, "Performance of an AUV Navigation System at Arctic Latitudes," *IEEE Journal of Oceanic Engineering*, vol. 30, no. 2, pp. 443–454, 2005. doi: 10.1109/JOE.2004.838336

[24] B. Jalving, J. E. Faugstadmo, K. Vestgard, O. Hegrenaes, O. Engelhardtsen, and B. Hyland, "Payload sensors, navigation and risk reduction for auv under ice surveys," in *OCEANS*. IEEE, 2008. doi: 10.1109/AUV.2008.5290525 pp. 1–8.

[25] M. V. Jakuba, C. N. Roman, H. Singh, C. Murphy, C. Kunz, C. Willis, T. Sato, and R. A. Sohn, "Long-baseline acoustic navigation for under-ice autonomous underwater vehicle operations," *Journal of Field Robotics*, vol. 25, no. 11-12, pp. 861–879, 2008. doi: 10.1002/rob.20250

[26] A. Plueddemann, A. Kukulya, R. Stokey, and L. Freitag, "Autonomous Underwater Vehicle Operations Beneath Coastal Sea Ice," *IEEE/ASME transactions on mechatronics*, vol. 17, no. 1, pp. 54–64, 2011. doi: 10.1109/TMECH.2011.2174798

[27] P. Wadhams, N. Hughes, and J. Rodrigues, "Arctic sea ice thickness characteristics in winter 2004 and 2007 from submarine sonar transects," *Journal of Geophysical Research: Oceans*, vol. 116, no. C8, 2011. doi: 10.1029/2011JC006982

[28] A. Kukulya, J. Bellingham, J. Kaeli, C. Reddy, M. Godin, and R. Conmy, "Development of a propeller driven long range autonomous underwater vehicle (LRAUV) for under-ice mapping of oil spills and environmental hazards: An Arctic

Domain Center of Awareness project (ADAC)," in *IEEE/OES Autonomous Underwater Vehicles (AUV)*. IEEE, 2016. doi: 10.1109/AUV.2016.7778655 pp. 95–100.

[29] C. Robotic, "Solus Long-Range Autonomous Underwater Vehicle," https://www.cellula.com/solus-lr, accessed: 16-April-2020.

[30] D. Roper, C. A. Harris, G. Salavasidis, M. Pebody, R. Templeton, T. Prampart, M. Kingsland, R. Morrison, M. Furlong, A. B. Phillips, and S. McPhail, "Autosub Long Range 6000: A Multiple-Month Endurance AUV for Deep-Ocean Monitoring and Survey," *IEEE Journal of Oceanic Engineering*, pp. 1–13, 2021. doi: 10.1109/JOE.2021.3058416

[31] D. T. Roper, A. B. Phillips, C. A. Harris, G. Salavasidis, M. Pebody, R. Templeton, S. V. S. Amma, M. Smart, and S. McPhail, "Autosub Long Range 1500: An Ultra-Endurance AUV with 6000 Km Range," in *OCEANS–Aberdeen*. IEEE, June 2017. doi: 10.1109/OCEANSE.2017.8084928 pp. 1–5.

[32] D. L. Rudnick, R. E. Davis, C. C. Eriksen, D. M. Fratantoni, and M. J. Perry, "Underwater Gliders for Ocean Research," *Marine Technology Society Journal*, vol. 38, no. 2, pp. 73–84, 2004.

[33] G. Salavasidis, A. Munafò, D. Fenucci, C. A. Harris, T. Prampart, R. Templeton, M. Smart, D. T. Roper, M. Pebody, S. D. McPhail, E. Rogers, and A. B. Phillips, *Ultra-Endurance AUVs: energy requirements and terrain-aided navigation*. The Institution of Engineering and Technology, 2020, doi: 10.1049/SBRA525E_ch.

[34] G. Salavasidis, "Terrain-Aided Navigation for Long-Range AUVs Operating in Uncertain Environments," Ph.D. dissertation, University of Southampton, July 2019.

[35] L. Paull, S. Saeedi, M. Seto, and H. Li, "AUV navigation and localization: A review," *Oceanic Engineering, IEEE Journal of*, vol. 39, no. 1, pp. 131–149, 2014. doi: 10.1109/JOE.2013.2278891

[36] L. Medagoda, S. B. Williams, O. Pizarro, J. C. Kinsey, and M. V. Jakuba, "Mid-water current aided localization for autonomous underwater vehicles," *Autonomous Robots*, vol. 40, no. 7, pp. 1207–1227, 2016. doi: 10.1007/s10514-016-9547-3

[37] G. Salavasidis, A. Munafò, D. Fenucci, C. A. Harris, T. Prampart, R. Templeton, M. Smart, D. T. Roper, M. Pebody, P. E. Abrahamsen, S. D. McPhail, E. Rogers, and A. B. Phillips, "Terrain-Aided Navigation for Long-Range AUVs in Dynamic Under-Mapped Environments," *Journal of Field Robotics*, vol. 38, no. 3, pp. 402–428, 2021. doi: https://doi.org/10.1002/rob.21994. [Online]. Available: https://onlinelibrary.wiley.com/doi/abs/10.1002/rob.21994

[38] G. Salavasidis, A. Munafò, C. A. Harris, T. Prampart, R. Templeton, M. Smart, D. T. Roper, M. Pebody, S. D. McPhail, E. Rogers, and A. B. Phillips, "Terrain–Aided Navigation for Long–Endurance and Deep–Rated Autonomous Underwater Vehicles," *Journal of Field Robotics*, vol. 36, no. 2, pp. 447–474, 2019. doi: 10.1002/rob.21832

[39] J. Melo and A. Matos, "Survey on advances on terrain based navigation for autonomous underwater vehicles," *Ocean Engineering*, vol. 139, pp. 250–264, 2017. doi: 10.1016/j.oceaneng.2017.04.047

[40] D. K. Meduna, *Terrain relative navigation for sensor-limited systems with application to underwater vehicles*. PhD thesis, Stanford University, 2011.

[41] B. Claus and R. Bachmayer, "Terrain-aided Navigation for an Underwater Glider," *Journal of Field Robotics*, vol. 32, no. 7, pp. 935–951, 2015. doi: 10.1002/rob.21563

[42] F. C. Teixeira, J. Quintas, P. Maurya, and A. Pascoal, "Robust particle filter formulations with application to terrain-aided navigation," *International Journal of Adaptive Control and Signal Processing*, vol. 31, no. 4, pp. 608–651, 2017. doi: 10.1002/acs.2692

[43] K. B. Anonsen and O. Hallingstad, "Terrain Aided Underwater Navigation using Point Mass and Particle Filters," in *Proceedings of the IEEE/ION Position Location and Navigation Symposium*. IEEE, Coronado, CA, USA, 2006. doi: 10.1109/PLANS.2006.1650705 pp. 1027–1035.

[44] L. Mayer, M. Jakobsson, G. Allen, B. Dorschel, R. Falconer, V. Ferrini, G. Lamarche, H. Snaith, and P. Weatherall, "The nippon foundation—gebco seabed 2030 project: The quest to see the world's oceans completely mapped by 2030," *Geosciences*, vol. 8, no. 2, p. 63, 2018.

[45] P. E. Abrahamsen, "Gridded bathymetric compilation of selected areas within the orkney passage, scotia sea from multibeam echosounder data collected by multiple vessels (1989 — 2017) [data set]," in *UK Polar Data Centre*. Natural Environment Research Council, UK Research and Innovation, 2020, doi: 10.5285/1221BBBD-843E-46D6-B96C-9C559AECFB20.

[46] G. Madec, "NEMO Ocean Engine," *Note du Pole de modelisation, Institut Pierre-Simon Laplace (IPSL), France*, vol. 27, pp. 1288–1619, 2008.

[47] M. Jakobsson, L. Mayer, B. Coakley, J. A. Dowdeswell, S. Forbes, B. Fridman, H. Hodnesdal, R. Noormets, R. Pedersen, M. Rebesco *et al.*, "The International Bathymetric Chart of the Arctic Ocean (IBCAO) Version 3.0," *Geophysical Research Letters*, vol. 39, no. 12, 2012.

[48] S. Karaman and E. Frazzoli, "Sampling-Based Algorithms for Optimal Motion Planning," *The international journal of robotics research*, vol. 30, no. 7, pp. 846–894, 2011. doi: 10.1177/0278364911406761

[49] G. Salavasidis, A. Munafò, C. A. Harris, S. D. McPhail, E. Rogers, and A. B. Phillips, "Towards Arctic AUV Navigation," *IFAC-PapersOnLine*, vol. 51, no. 29, pp. 287–292, 2018. doi: 10.1016/j.ifacol.2018.09.517

[50] M. E. Furlong, D. Paxton, P. Stevenson, M. Pebody, S. D. McPhail, and J. Perrett, "Autosub Long Range: A long range deep diving AUV for ocean monitoring," in *Autonomous Underwater Vehicles (AUV), 2012 IEEE/OES*. IEEE, 2012, pp. 1–7.

[51] A. B. Phillips, G. Salavasidis, M. Kingsland, C. Harris, M. Pebody, D. Roper, R. Templeton, S. McPhail, T. Prampart, T. Wood, R. Taylor, and T. Jones, "Autonomous Surface/Subsurface Survey System Field Trials," in *2018 IEEE/OES Autonomous Underwater Vehicles (AUV)*. IEEE, 2018. doi: 10.1109/AUV.2018.8729740

[52] N. P. Fofonoff and R. C. Millard, "Algorithms for the computation of fundamental properties of seawater." *UNESCO Technical Papers in Marine Science 44.*, 1983.

[53] iXblue, "OCTANS Fiber-Optic Gyrocompass," https://www.ixblue.com/sites/default/files/2020-02/Octans_2019.pdf, accessed: 31-March-2020.

[54] F. C. Teixeira, "Terrain-Aided Navigation and Geophysical Navigation of Autonomous Underwater Vehicles," Ph.D. dissertation, Dynamical Systems and Ocean Robotics Lab, Lisbon, 2007.

[55] T. Schon, F. Gustafsson, and P.-J. Nordlund, "Marginalized Particle Filters for Mixed Linear/Nonlinear State-Space Models," *IEEE Transactions on signal processing*, vol. 53, no. 7, pp. 2279–2289, 2005. doi: 10.1109/TSP.2005.849151

[56] P. Desmet, "Effects of Interpolation Errors on the Analysis of DEMs," *Earth Surface Processes and Landforms: The Journal of the British Geomorphological Group*, vol. 22, no. 6, pp. 563–580, 1997.

[57] R. Hare, B. Eakins, and C. Amante, "Modelling Bathymetric Uncertainty," *The International Hydrographic Review*, no. 6, 2011.

[58] S. Wechsler, "Uncertainties associated with digital elevation models for hydrologic applications: a review," *Hydrology and Earth System Sciences*, vol. 11, no. 4, pp. 1481–1500, 2007. doi: 10.5194/hess-11-1481-2007

[59] M. Jakobsson, B. Calder, and L. Mayer, "On the Effect of Random Errors in Gridded Bathymetric Compilations," *Journal of Geophysical Research: Solid Earth*, vol. 107, no. B12, 2002.

[60] K. Marks and W. Smith, "An uncertainty model for deep ocean single beam and multibeam echo sounder data," *Marine Geophysical Researches*, vol. 29, no. 4, pp. 239–250, 2008.

[61] P. A. Burrough, "Principles of Geographical Information Systems for Land Resources Assessment," 1986.

[62] Q. Guo, W. Li, H. Yu, and O. Alvarez, "Effects of Topographic Variability and LIDAR Sampling Density on several DEM Interpolation Methods," *Photogrammetric Engineering & Remote Sensing*, vol. 76, no. 6, pp. 701–712, 2010.

[63] W. H. Smith and D. T. Sandwell, "Global Sea Floor Topography from Satellite Altimetry and Ship Depth Soundings," *Science*, vol. 277, no. 5334, pp. pp. 1956–1962, 1997.

[64] M. Jakobsson, R. Macnab, L. Mayer, R. Anderson, M. Edwards, J. Hatzky, H. W. Schenke, and P. Johnson, "An Improved Bathymetric Portrayal of the Arctic Ocean: Implications for Ocean Modeling and Geological, Geophysical and Oceanographic Analyses," *Geophysical Research Letters*, vol. 35, no. 7, 2008.

[65] A. J. Häusler, A. Saccon, A. M. Pascoal, J. Hauser, and A. P. Aguiar, "Cooperative AUV Motion Planning using Terrain Information," in *MTS/IEEE OCEANS–Bergen*. IEEE, 2013, pp. 1–10.

[66] Y. Li, T. Ma, P. Chen, Y. Jiang, R. Wang, and Q. Zhang, "Autonomous Underwater Vehicle Optimal Path Planning Method for Seabed Terrain Matching Navigation," *Ocean Engineering*, vol. 133, pp. 107–115, 2017.

[67] G. Salavasidis, C. Harris, S. McPhail, A. B. Phillips, and E. Rogers, "Terrain-Aided Navigation for long range AUV operations at Arctic latitudes," in *Autonomous Underwater Vehicles (AUV), 2016 IEEE/OES*. IEEE, 2016. doi: 10.1109/AUV.2016.7778658 pp. 115–123.

[68] P. Pasnani and M. L. Seto, "Terrain-Based Localization and Mapping for Autonomous Underwater Vehicles using Particle Filters with Marine Gravity Anomalies," *IFAC-PapersOnLine*, vol. 51, no. 29, pp. 354–359, 2018. doi: 10.1016/j.ifacol.2018.09.498

[69] A. Munafò, F. Fanelli, G. Salavasidis, A. Storto, and P. Oddo, "Navigation of AUVs based on Ocean Fields Variability," in *OCEANS–Marseille*. IEEE, June 2019. doi: 10.1109/OCEANSE.2019.8867309 pp. 1–9.